

Physical machine learning outperforms “human learning” in Quantum Chemistry

Anton V. Sinitskiy, Vijay S. Pande

Department of Bioengineering, Stanford University, Stanford CA 94305

Two types of approaches to modeling molecular systems have demonstrated high practical efficiency. Density functional theory (DFT), the most widely used quantum chemical method, is a physical approach predicting energies and electron densities of molecules. Recently, numerous papers on machine learning (ML) of molecular properties have also been published. ML models greatly outperform DFT in terms of computational costs, and may even reach comparable accuracy, but they are missing physicality — a direct link to Quantum Physics — which limits their applicability. Here, we propose an approach that combines the strong sides of DFT and ML, namely, physicality and low computational cost. We derive general equations for exact electron densities and energies that can naturally guide applications of ML in Quantum Chemistry. Based on these equations, we build a deep neural network that can compute electron densities and energies of a wide range of organic molecules not only much faster, but also closer to exact physical values than current versions of DFT. In particular, we reached a mean absolute error in energies of molecules with up to eight non-hydrogen atoms as low as 0.9 kcal/mol relative to CCSD(T) values, noticeably lower than those of DFT (approaching ~2 kcal/mol) and ML (~1.5 kcal/mol) methods. A simultaneous improvement in the accuracy of predictions of electron densities and energies suggests that the proposed approach describes the physics of molecules better than DFT functionals developed by “human learning” earlier. Thus, physics-based ML offers exciting opportunities for modeling, with high-theory-level quantum chemical accuracy, of much larger molecular systems than currently possible.

From the Schrödinger equation (and relativistic corrections to it), one could in principle compute any physico-chemical property of any molecular system. A multitude of quantum chemical methods were developed to approximately solve the Schrödinger equation, with density functional theory (DFT)^{1,2} being nowadays the most widely used method. DFT computes approximate values of energies E and electron densities $\rho(\mathbf{r})$ of molecules (section S1), providing the basis for explanations and predictions of various properties of chemical compounds. DFT is based on the Hohenberg-Kohn theorems¹ claiming that E and $\rho(\mathbf{r})$ for the ground state of a molecule can be computed variationally, by minimizing a certain functional $E[\cdot]$ of $\rho(\mathbf{r})$. An explicit analytical expression for $E[\cdot]$ is unknown, and a multitude of versions of DFT, based on various approximations, have been proposed (in other words, found by “human learning”). Analysis of $\rho(\mathbf{r})$ computed with various DFT functionals for several atoms and ions demonstrated that some recent functionals do not improve (or even worsen) the accuracy of $\rho(\mathbf{r})$ predictions.³ Our validation of various functionals on a larger set of molecules shows that the DFT functionals best at predicting E are not the best at predicting $\rho(\mathbf{r})$, and vice versa (section S2). Taking into account the existing practice to fit and test new DFT functionals on E , but not $\rho(\mathbf{r})$ datasets, these observations may signal that many DFT functionals are overfitted to E , and their reported accuracy may be not transferable to some other classes of molecules or conformations. In addition to the concerns about the accuracy, practical applications of DFT are limited to molecular systems with tens or hundreds of atoms because of a quick polynomial growth in the cost of DFT computations with the size of a modeled system.

Recently, many authors used machine learning (ML) for much faster computations of E and some other molecular properties (partial charges on atoms, polarizabilities, HOMO-LUMO gaps, forces acting on atoms, etc.).⁴⁻²¹ However, these works often treat a molecule as a “bag of features”. Currently used descriptors of molecules do

not have a transparent connection to the basic physical concepts derived from the Schrödinger equation. For this reason, such approaches might be devoid of physics, and the criticism of ML²² as “black boxes” and “curve-fitting” seems totally applicable to them.

In this work, we put forward a theoretically strict approach to ML in Quantum Chemistry. From the Hohenberg-Kohn theorems, we derive the following equations for the ground state energy E and electron density $\rho(\mathbf{r})$ of an arbitrary molecular system:

$$\rho(\mathbf{r}) = \rho_0(\mathbf{r}) + \Delta\rho[\rho_0(\mathbf{r})],$$

$$E = E_0 + \Delta E[\rho_0(\mathbf{r})],$$

where $\rho_0(\mathbf{r})$ is an electron density variationally computed with a specific DFT functional or with the HF theory, E_0 is the corresponding energy, and $\Delta\rho[\cdot]$ and $\Delta E[\cdot]$ are a function-to-function and function-to-scalar (functional) mappings, respectively, each of which can be approximated with ML (for a derivation, see Section S3). These equations have two implications of fundamental importance for ML in Quantum Chemistry. First, it is an approximate electron density $\rho_0(\mathbf{r})$ computed with HF or a specific DFT method that can serve as a natural descriptor of a molecular system for the purpose of ML. Second, it is not necessary to use ML to learn the Hohenberg-Kohn functional $E[\cdot]$ itself and iteratively minimize it; instead, one can learn $\Delta\rho[\cdot]$ and $\Delta E[\cdot]$, and use them for direct, non-iterative, single-shot predictions of E and $\rho(\mathbf{r})$.

Three-dimensional (3D) convolutional (Conv) deep neural networks (DNNs) are a natural ML model for this purpose (Fig. 1). Recently, DNNs have been successfully applied to various tasks in ML, in particular, computer vision and other manipulations with 2D and 3D data, and in some cases even outperformed humans in these tasks. The input density $\rho_0(\mathbf{r})$ and the output correction to the density $\Delta\rho[\rho_0(\mathbf{r})]$ are 3D objects naturally admitting a 3D grid representation (so-called "cube representation"), a format that a 3D Conv DNN can directly work with. A 3D cube representation is more flexible than finite basis set expansions typically used in Quantum Chemistry, because it is not restricted to specific analytical expressions, and may provide higher accuracy in predicting $\Delta\rho[\rho_0(\mathbf{r})]$, and thereby $\rho(\mathbf{r})$, especially in the regions of low electron density important for non-covalent interactions. The “conv3d” transformation in the first layer of a DNN can compute, among other entities, gradients and Hessians of the density with respect to \mathbf{r} , the variables that often appear in analytical approximations in Quantum Chemistry, and play key roles in previously developed advanced (GGA, meta-GGA and hybrid) DFT functionals. At the last layer of the DNN, the use of “conv3d” (for $\Delta\rho$) or “average_pooling3d” (for ΔE) operations is a natural way to estimate integrals present in the analytical expressions for $\Delta\rho[\cdot]$ and $\Delta E[\cdot]$ [Fig. 1b,c; eqs. (S7), (S8)]. Finally, the mentioned analytical expressions consist of similar building blocks, or “precursors” [schematically denoted as $\delta E/\delta\rho$, $(\delta^2 E/\delta\rho^2)^{-1}$ and $\Delta\mu$, Fig. 1] that need to be computed first, and only after that do computations fork into two paths leading to $\Delta\rho$ and ΔE . The corresponding forking architecture of DNN is not only physically motivated, but also, from the viewpoint of ML, prevents overfitting of the network to the specific task of predicting E , and uses the information on $\rho(\mathbf{r})$ as a physics-based regularizer of the DNN. Overall, a physically driven approach to Quantum Chemistry can mesh well with DNN structures. Intermediate layers in DNNs can learn physically well-defined concepts or “precursors” of the output, and first and last layers can perform operations (such as differentiation or integration) that are present in “humanly learned” approaches to the problem.

To validate this research philosophy, we have developed a “physical machine learning in Quantum Chemistry” (PML-QC) model, which is a 3D Conv DNN that can compute E and $\rho(\mathbf{r})$ of a large set of organic molecules (Fig.

1; see also Section S4). The model was trained in two stages: first, on cheaper and not-so-accurate DFT data, resulting in the PML-QC_{DFT} version of the model (Fig. 2), and after that, on more accurate, but much more expensive (and therefore more scarce) CCSD [for $\rho(\mathbf{r})$] and CCSD(T) (for E) data, resulting in the PML-QC_{CCSD} version of the model (Fig. 3, Table 1). On test sets of molecules, not used for training or validation, PML-QC_{DFT} demonstrated the accuracy comparable to that of best versions of DFT, and PML-QC_{CCSD} a performance significantly better than DFT (see Section S4 for details). In particular, the mean absolute error in E predicted with PML-QC_{CCSD} was as low as ~ 0.9 kcal/mol (Table 1), below the psychological threshold of “thermochemical accuracy” of ~ 1 kcal/mol required for practical applications, and below the accuracy of 1.5 kcal/mol reported in the only (to the best of our knowledge) paper that compared E predicted with ML to CCSD(T)-level E (and not DFT-level E) for a large dataset of molecules (see Section S5).²⁰ We attribute this excellent performance of the model primarily to the use of an approximate electron density as the input to a neural network, which, even at the HF level, is a more physically meaningful and information rich representation of a molecule than previously used “bag of atom/bonds” featurizations.

Thus, in this work we demonstrate that physics-based ML in Quantum Chemistry can outperform “humanly learned” versions of DFT, the most widely used quantum chemical method nowadays, in the accuracy of E and $\rho(\mathbf{r})$ predictions and the speed of computations, all at the same time. Our theoretical analysis (in particular, the formulas given above) explains the astonishing fact that a single input channel with an approximate density $\rho_0(\mathbf{r})$ was sufficient for the network to predict both E and $\rho(\mathbf{r})$, and no other input channels [e.g., with atomic numbers, geometries, electrostatic potentials, gradients and Hessians of $\rho_0(\mathbf{r})$] were required. Not only does our framework predict $\rho(\mathbf{r})$ as a physical measurable, but also uses $\rho(\mathbf{r})$ for regularization of the neural network, pushing it towards learning physics rather than curve fitting. Moreover, the delta ML approach – the use of ML to predict differences, rather than absolute values, in the interests of higher accuracy of predictions – emerges naturally in this theoretical framework. Similarly to post-HF methods, such as MP2 or CCSD, PML-QC can build on an approximate HF solution; unlike post-HF methods, it may also build on DFT solutions, and accounting for correlations does not create a computational bottleneck in PML-QC. We foresee wide-scale applications of the approach proposed here (after certain technical developments) to computer modeling of various large molecular systems, including CCSD(T)-level *ab initio* Molecular Dynamics and Monte Carlo simulations of biomolecular or artificial material systems, and highly accurate and fast modeling of excited states of molecules and chemical reactions involving bond breaking and formation.

Conflict of interests. V.S.P. is a consultant & SAB member of Schrodinger, LLC and Globavir, sits on the Board of Directors of Apeel Inc, Asimov Inc, BioAge Labs, Freenome Inc, Omada Health, Patient Ping, Rigetti Computing, and is a General Partner at Andreessen Horowitz.

Acknowledgements. The authors would like to thank other members of the Pande lab, in particular, Dr. Peter Eastman and Dr. Joseph Gomes, as well as Prof. Lee-Ping Wang, for valuable feedback on our results and manuscript. The Pande Group acknowledges the generous support of Dr. Anders G. Frøseth and Mr. Christian Sundt for our work on machine learning. The Pande Group is broadly supported by grants from the NIH (R01 GM062868 and U19 AI109662) as well as gift funds and contributions from Folding@home donors.

Table 1. Mean absolute errors (MAEs) in energies predicted by PML-QC after the first stage of training (PML-QC_{DFT}), in comparison to CCSD(T) energies (section S2), were nearly the same as MAEs in the original QM9 energies²³ computed with DFT (~4 kcal/mol). After transfer learning on CCSD(T) energies, the MAEs of the neural network (PML-QC_{CCSD}) dropped to ~0.9 kcal/mol.

Subset / molecule	QM9 error, kcal/mol	PML-QC _{DFT} error, kcal/mol	PML-QC _{CCSD} error, kcal/mol
Training (3612 molecules, indices up to 6000)	4.8	5.1	0.88
Validation (463 molecules, indices up to 6000)	4.3	4.5	0.88
Test (430 molecules, indices up to 6000)	3.5	3.7	0.86

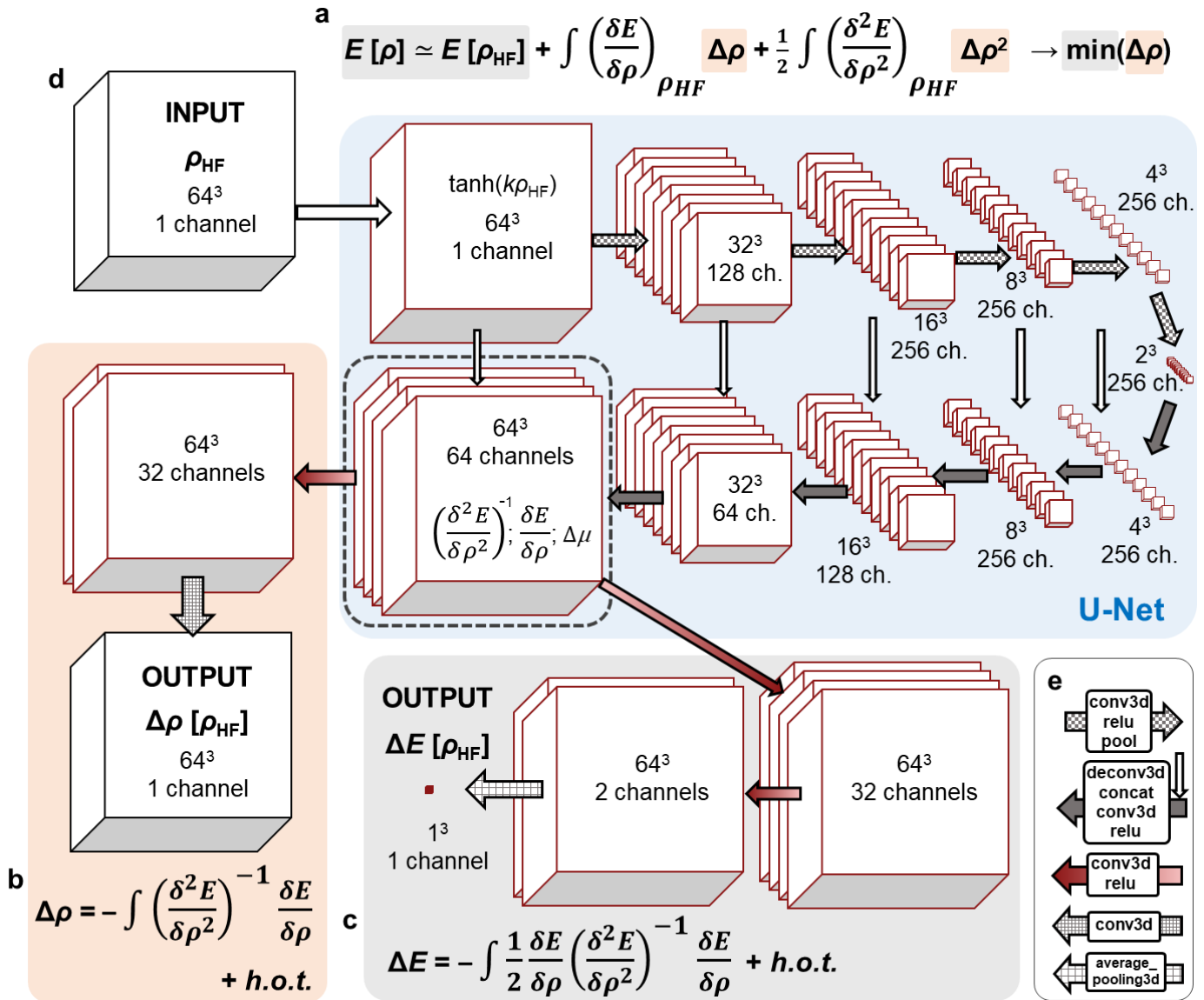
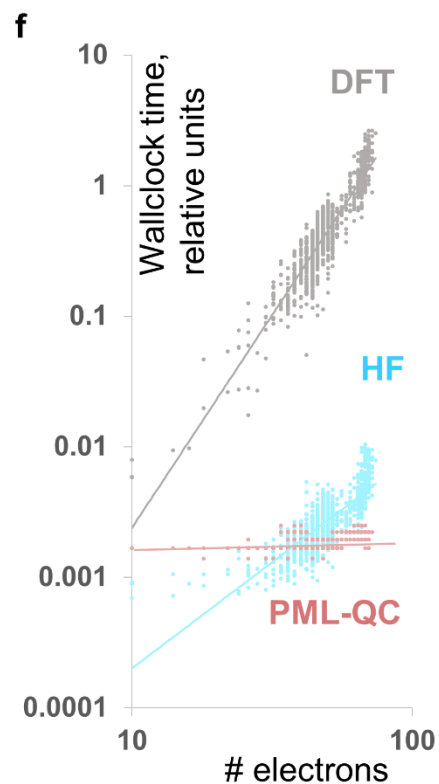
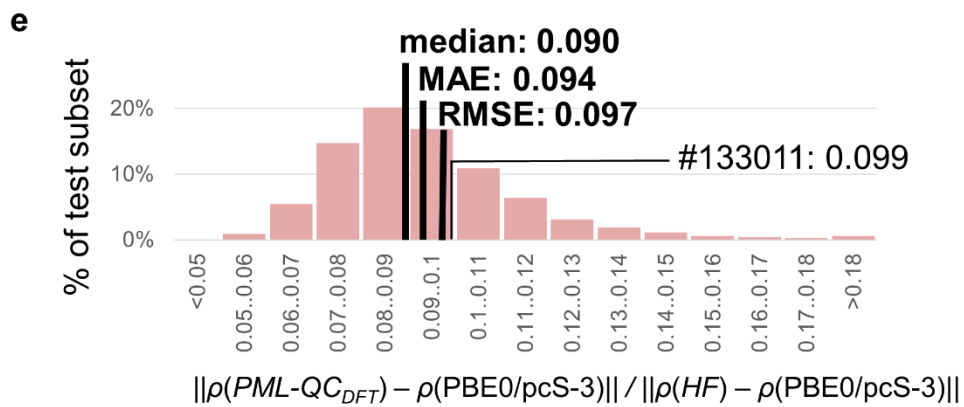
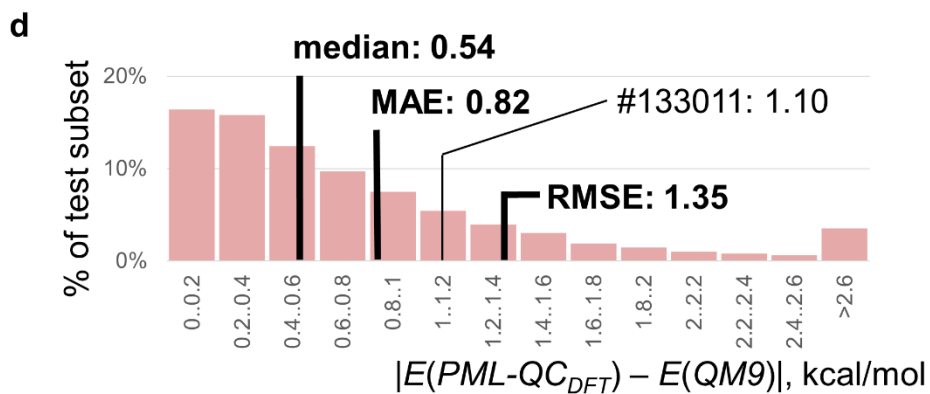
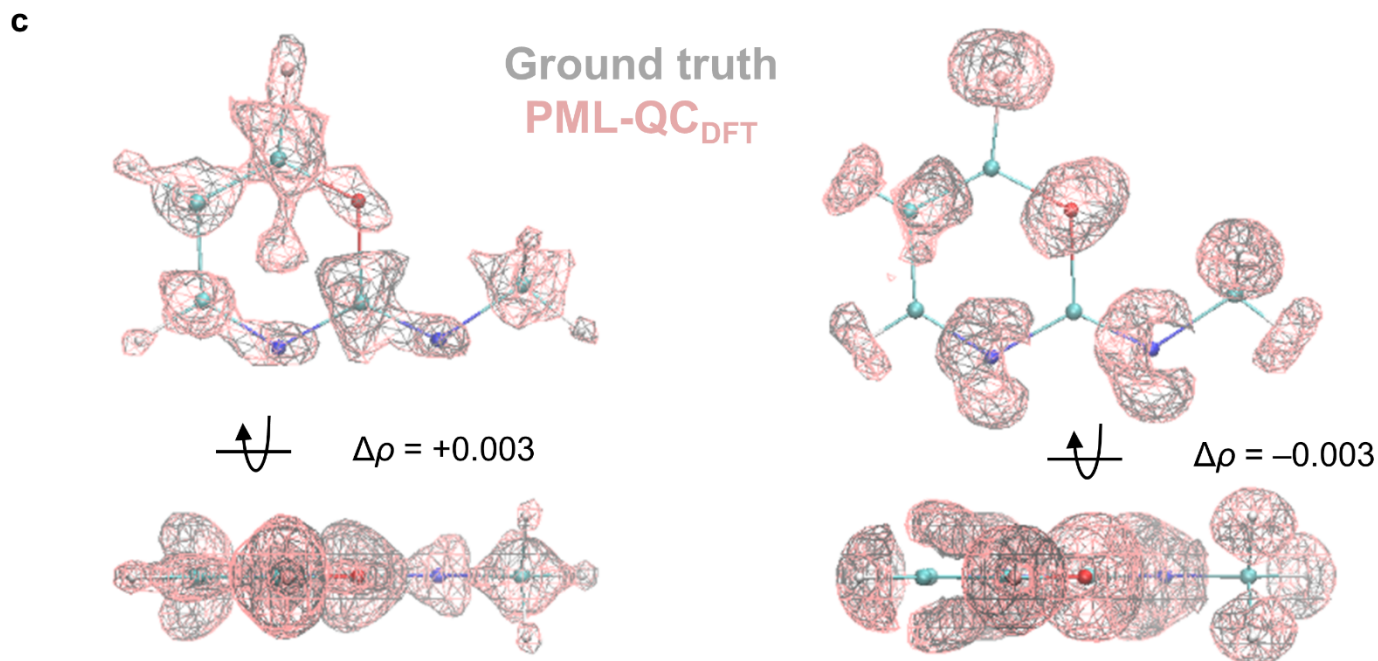
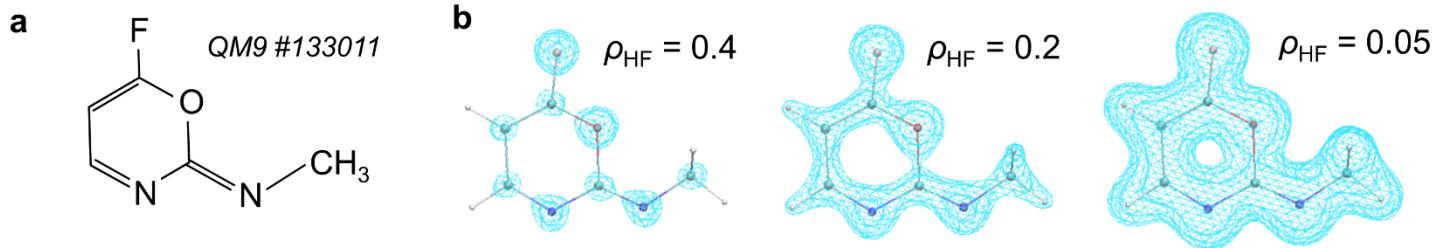


Fig. 1. Proposed machine learning approach to Quantum Chemistry has deep physical motivation. (a) The Hohenberg-Kohn theorems state the existence of the exact density functional $E[\rho]$ of the electron density $\rho(\mathbf{r})$. Our analysis is based on a functional Taylor series expansion of $E[\rho]$ in the vicinity of an approximate electron density [for example, a density computed with the Hartree-Fock (HF) theory $\rho_{\text{HF}}(\mathbf{r})$]. (b) The correction to the electron density $\Delta\rho(\mathbf{r})$ that minimizes the exact density functional $E[\rho]$ can be expressed as the value of a function-to-function mapping $\Delta\rho[\cdot]$ evaluated at $\rho_{\text{HF}}(\mathbf{r})$. This mapping $\Delta\rho[\cdot]$ is uniquely defined by $E[\cdot]$; *h.o.t.*, higher order terms. (c) Similarly, the correction to the energy $\Delta E = E[\rho] - E[\rho_{\text{HF}}]$ can be computed as the value of a functional $\Delta E[\cdot]$ at $\rho_{\text{HF}}(\mathbf{r})$. This functional $\Delta E[\cdot]$ is also uniquely defined by $E[\cdot]$. (b,c) Instead of finding $E[\cdot]$ better than in the existing DFT methods, we suggest that a deep neural network (DNN) be trained to directly approximate $\Delta\rho[\cdot]$ and $\Delta E[\cdot]$. (d) The architecture of the reported DNN for PML-QC follows this motivation: $\rho_{\text{HF}}(\mathbf{r})$ (in a cube file representation, on a $64 \times 64 \times 64$ grid) is the only input to the network; the U-Net^{24,25} part, *blue*, serves to learn high-level features characterizing the modeled molecule, *gray dashed box* [presumably features related to the first-order functional derivative $\delta E/\delta\rho$, the resolvent $(\delta^2 E/\delta\rho^2)^{-1}$, and the chemical potential $\Delta\mu$, see Eqs. (S7) and (S8)]. Then, the network forks into two paths, one of which leads to the output electron density, *peach*, and the other one to the output energy, *gray*. This forking architecture is justified by the fact that the equations for $\Delta\rho$ and ΔE (see b,c) consist of similar building blocks. “ch.”, shorthand for “channels”. (e) Legend for the arrows in the DNN architecture. Panels (a,b,c) show sketches of formulas; for mathematically strict expressions, see Eqs. (S5), (S7) and (S8).



◀ **Fig. 2. PML-QC_{DFT}, the network we trained on DFT data, predicts electron densities and energies with the accuracy comparable to DFT, but does so several orders of magnitude faster.** (a) Molecules from the QM9 database (nearly 134,000 organic molecules) were used for training, validation and testing. Performance of PML-QC_{DFT} is illustrated here for the molecule with QM9 index 133011. This molecule belongs to the test subset, has a large QM9 index, is diverse in terms of elemental composition and functional groups, and can serve as a conservative example of the excellent performance of PML-QC_{DFT} (the accuracies of the energy and density predictions for it are somewhat worse than on average for the test set). (b) Approximate electron density $\rho_{HF}(\mathbf{r})$ is quickly computed with HF in a small basis set (HF/cc-pVDZ). Isosurfaces for $\rho_{HF}(\mathbf{r}) = 0.4, 0.2,$ and 0.05 shown in *light blue* (here and below, electron densities are given in Hartree units). See also Movie S1. (c) Correction to the electron density $\Delta\rho(\mathbf{r})$ predicted by PML-QC_{DFT}, *pink*, is very close to the ground truth value (computed with PBE0/pcS-3), *gray*. See also Movie S2. (d) Distribution diagram for the absolute differences of predicted and ground truth [from DFT, B3LYP/6-31G(2df,p)] values of ΔE , for molecules in the test subset (test set 1, see Sections S4.3-4.4). In a half of all molecules, the differences are below 0.54 kcal/mol, and the distribution density decays fast with energy differences. (e) The same, for the *L1* measure of the deviations of predicted electron densities from PBE0/pcS-3 densities, divided by the *L1* measure of the deviations of HF/cc-pVDZ densities from PBE0/pcS-3 densities. In most cases, the electron densities predicted with PML-QC_{DFT} are ~ 10 – 12 times closer to the ground truth densities than the HF densities. (f) Scaling of the wallclock time to run DFT, PML-QC and HF computations with the number of electrons for various QM9 molecules (note log scales on both axes) shows that the cost of PML-QC computations is not a computational bottleneck for molecules of practically important sizes (Section S4.5).

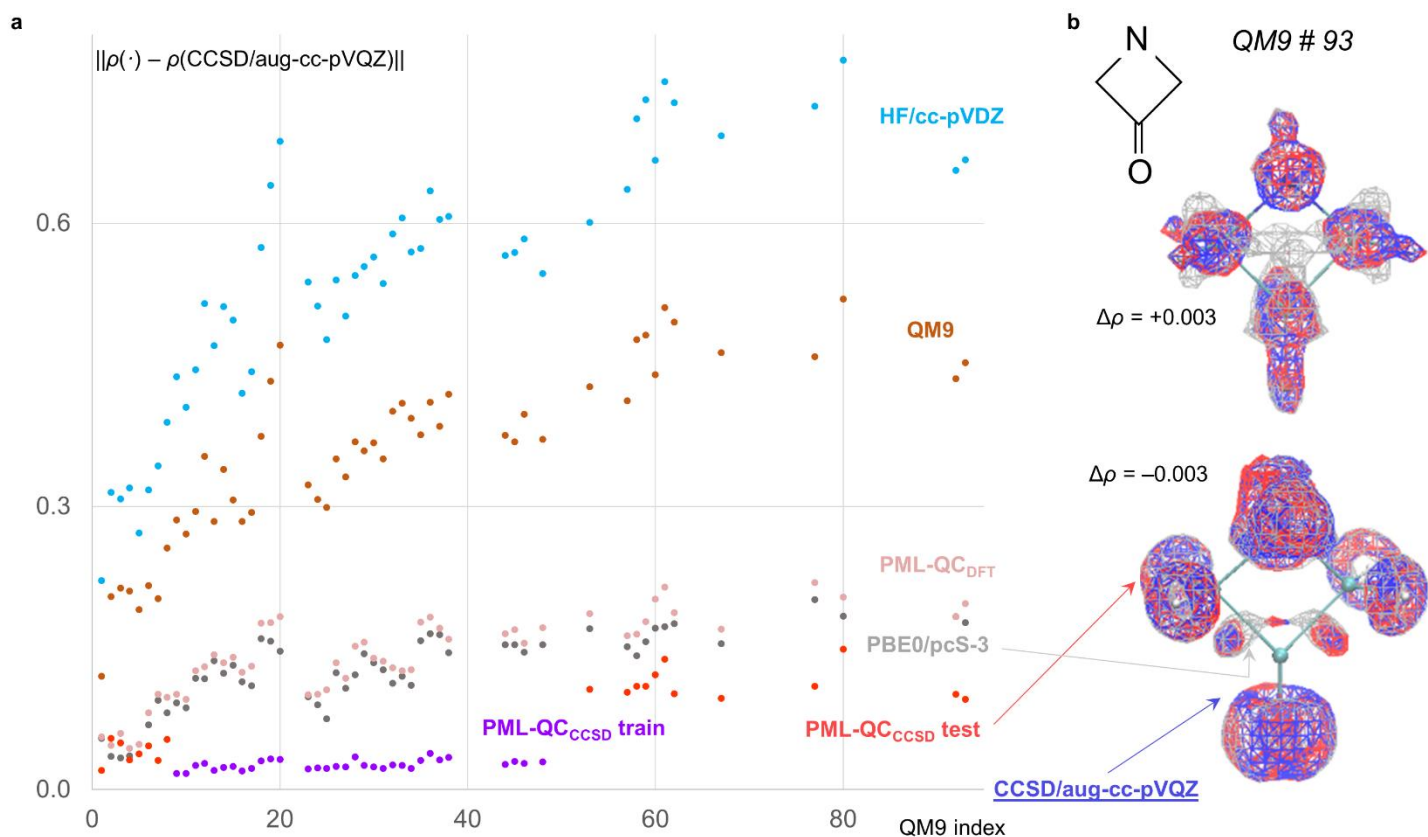


Fig. 3. Transfer learning on CCSD electron densities significantly improves the performance of the neural network (PML-QC_{CCSD}). (a) *L1* measure of the difference of electron densities predicted with HF/cc-pVDZ (*light blue*), B3LYP/6-31G(2df,p) (*orange*), PBE0/pcS-3 (*gray*), PML-QC_{DFT} (*pink*) and PML-QC_{CCSD} (training set, *violet*, test set, *red*) from CCSD/aug-cc-pVQZ electron densities. (b) Comparison of the electron densities of molecule with QM9 index 93 computed with DFT (PBE0/pcS-3, here and below $\Delta\rho(\mathbf{r})$ shown for clarity, *gray*), CCSD/aug-cc-pVQZ (*blue*), and PML-QC_{CCSD} (*red*) demonstrates that the output of PML-QC_{CCSD} is much closer to CCSD than DFT results. See also Movie S3.

References

- 1 Hohenberg, P. & Kohn, W. Inhomogeneous Electron Gas. *Phys. Rev.* **136**, B864 (1964).
- 2 Becke, A. D. Perspective: Fifty years of density-functional theory in chemical physics. *J. Chem. Phys.* **140**, 18A301, doi:10.1063/1.4869598 (2014).
- 3 Medvedev, M. G., Bushmarinov, I. S., Sun, J., Perdew, J. P. & Lyssenko, K. A. Density functional theory is straying from the path toward the exact functional. *Science* **355**, 49-52, doi:10.1126/science.aah5975 (2017).
- 4 Smith, J. S., Isayev, O. & Roitberg, A. E. ANI-1, A data set of 20 million calculated off-equilibrium conformations for organic molecules. *Sci. Data* **4**, 170193, doi:10.1038/sdata.2017.193 (2017).
- 5 Smith, J. S., Isayev, O. & Roitberg, A. E. ANI-1: an extensible neural network potential with DFT accuracy at force field computational cost. *Chem. Sci.* **8**, 3192-3203, doi:10.1039/c6sc05720a (2017).
- 6 Berau, T., DiStasio, R. A., Jr., Tkatchenko, A. & von Lilienfeld, O. A. Non-covalent interactions across organic and biological subsets of chemical space: Physics-based potentials parametrized from machine learning. *J. Chem. Phys.* **148**, 241706, doi:10.1063/1.5009502 (2018).
- 7 Bleiziffer, P., Schaller, K. & Riniker, S. Machine Learning of Partial Charges Derived from High-Quality Quantum-Mechanical Calculations. *J. Chem. Inf. Model.* **58**, 579-590, doi:10.1021/acs.jcim.7b00663 (2018).
- 8 Collins, C. R., Gordon, G. J., von Lilienfeld, O. A. & Yaron, D. J. Constant size descriptors for accurate machine learning models of molecular properties. *J. Chem. Phys.* **148**, 241718, doi:10.1063/1.5020441 (2018).
- 9 Dick, S. & Fernandez-Serra, M. Learning from the Density to Correct Total Energy and Forces in First Principle Simulations. *arXiv*, 1812.06572v06571 (2018).
- 10 Faber, F. A., Christensen, A. S., Huang, B. & von Lilienfeld, O. A. Alchemical and structural distribution based representation for universal quantum machine learning. *J. Chem. Phys.* **148**, 241717, doi:10.1063/1.5020710 (2018).
- 11 Li, H., Collins, C., Tanha, M., Gordon, G. J. & Yaron, D. J. A Density Functional Tight Binding Layer for Deep Learning of Chemical Hamiltonians. *J Chem Theory Comput* **14**, 5764-5776, doi:10.1021/acs.jctc.8b00873 (2018).
- 12 Nebgen, B. *et al.* Transferable Dynamic Molecular Charge Assignment Using Deep Neural Networks. *J. Chem. Theory Comput.* **14**, 4687-4698, doi:10.1021/acs.jctc.8b00524 (2018).
- 13 Pronobis, W., Tkatchenko, A. & Müller, K. R. Many-Body Descriptors for Predicting Molecular Properties with Machine Learning: Analysis of Pairwise and Three-Body Interactions in Molecules. *J Chem Theory Comput* **14**, 2991-3003, doi:10.1021/acs.jctc.8b00110 (2018).
- 14 Sifain, A. E. *et al.* Discovering a Transferable Charge Assignment Model Using Machine Learning. *J. Phys. Chem. Lett.* **9**, 4495-4501, doi:10.1021/acs.jpcclett.8b01939 (2018).
- 15 Unke, O. T. & Meuwly, M. A reactive, scalable, and transferable model for molecular energies from a neural network approach based on local information. *J. Chem. Phys.* **148**, 241708, doi:10.1063/1.5017898 (2018).
- 16 Zubatyuk, R., Smith, J. S., Leszczynski, J. & Isayev, O. Accurate and transferable multitask prediction of chemical properties with an atoms-in-molecule neural network. *chemRxiv*, 7151435.v7151432 (2018).
- 17 Chandrasekaran, A. *et al.* Solving the electronic structure problem with machine learning. *npj Computational Materials* **5**, 22 (2019).
- 18 Christensen, A. S., Faber, F. A. & von Lilienfeld, O. A. Operators in Machine Learning: Response Properties in Chemical Space. *J. Chem. Phys.* **150**, 064105 (2019).
- 19 Saucedo, H. E., Chmiela, S., Poltavsky, I., Müller, K. R. & Tkatchenko, A. Molecular force fields with gradient-domain machine learning: Construction and application to dynamics of small molecules with coupled cluster forces. *J Chem Phys* **150**, 114102, doi:10.1063/1.5078687 (2019).
- 20 Smith, J. S. *et al.* Approaching coupled cluster accuracy with a general-purpose neural network potential through transfer learning. *Nature Commun.* **10**, 2903, doi:10.1038/s41467-019-10827-4 (2019).
- 21 Wilkins, D. M. *et al.* Accurate molecular polarizabilities with coupled cluster theory and machine learning. *Proc Natl Acad Sci U S A* **116**, 3401-3406, doi:10.1073/pnas.1816132116 (2019).
- 22 Lemonick, S. Is machine learning overhyped? *Chemical & Engineering News* **96** (2018).
- 23 Ramakrishnan, R., Dral, P. O., Rupp, M. & von Lilienfeld, O. A. Quantum chemistry structures and properties of 134 kilo molecules. *Sci. Data* **1**, 140022, doi:10.1038/sdata.2014.22 (2014).
- 24 Ronneberger, O., Fischer, P. & Brox, T. in *Medical Image Computing and Computer-Assisted Intervention – MICCAI 2015. MICCAI 2015. Lecture Notes in Computer Science* Vol. 9351 (eds Navab N, Hornegger J, Wells W, & Frangi A) (Springer, Cham, 2015).
- 25 Farimani, A. B., Gomes, J. & Pande, V. S. Deep Learning the Physics of Transport Phenomena. *arxiv*, 1709.02432v02431 (2017).

Physical machine learning outperforms “human learning” in Quantum Chemistry

Anton V. Sinitskiy, Vijay S. Pande

Department of Bioengineering, Stanford University, Stanford CA 94305

SUPPLEMENTARY INFORMATION

S1. Definitions and basic relationships

In general, an isolated quantum mechanical system (for example, a molecule in vacuum) can be characterized by a wave function Ψ . A non-relativistic electronic wave function of a molecule with N electrons $\Psi(\mathbf{r}_1, \dots, \mathbf{r}_N, \tau_1, \dots, \tau_N)$ depends on $3N$ spatial coordinates $\mathbf{r}_1, \dots, \mathbf{r}_N$ and N spin coordinates τ_1, \dots, τ_N and can be found, together with the corresponding electronic energy E , from the stationary Schrödinger equation (after introducing the Born–Oppenheimer approximation to separate the motion of atomic nuclei):¹

$$\hat{H}_e \Psi(\mathbf{r}_1, \dots, \mathbf{r}_N, \tau_1, \dots, \tau_N) = E \Psi(\mathbf{r}_1, \dots, \mathbf{r}_N, \tau_1, \dots, \tau_N), \quad (\text{S1})$$

where \hat{H}_e is the electronic Hamiltonian for a given molecular system. For systems of practical interest, $N \gg 1$, making it difficult to work with wave functions because of their high dimensionality. On the contrary, the electron density, defined as

$$\rho(\mathbf{r}) = N \sum_{\tau_1} \dots \sum_{\tau_N} \int d\mathbf{r}_2 \dots \int d\mathbf{r}_N |\Psi(\mathbf{r}_1, \dots, \mathbf{r}_N, \tau_1, \dots, \tau_N)|^2, \quad (\text{S2})$$

is a function of only a three-dimensional vector \mathbf{r} , regardless of the size of the molecule. Hence, the electron density is much easier to deal with than the wave function from various viewpoints, including intuitive appreciation, graphical visualization and basis set expansions. This function shows how electrons are delocalized in a molecule, namely, where the probability to find an electron per unit volume is higher and where it is lower.

According to the Hohenberg–Kohn theorems,² the ground state energy E of a molecular system can be found by a minimization of a certain density functional $E[n(\mathbf{r})]$; the density n at which the minimum is achieved yields the ground state electron density $\rho(\mathbf{r})$:

$$E = \min_{n(\mathbf{r})} E[n(\mathbf{r})], \quad \rho(\mathbf{r}) = \operatorname{argmin}_{n(\mathbf{r})} E[n(\mathbf{r})]. \quad (\text{S3})$$

The Hohenberg–Kohn theorems serve as the motivation for Density Functional Theory (DFT), one of the main methods in Quantum Chemistry.²⁻⁷ DFT has been widely used by the scientific community because it offers a favorable tradeoff between the cost of computations and the accuracy of results, and deals with electron densities, which seem simpler for common (that is, based on macroscopic classical physics) intuition than multidimensional

wave functions. An exact expression for the density functional $E[\cdot]$ is not known. Numerous approximate functionals have been proposed, leading to multiple versions of DFT with various accuracy levels and computational costs.

Despite the importance of the electron density to DFT, very little work has been done on measuring the actual accuracy of DFT in predicting electron densities of molecules.⁸ One of the reasons is that 'exact' electron densities – that is, electron densities guaranteed to be much more accurate than those predicted from DFT, obtained either from experimental measurements or high-level quantum chemical computations with large basis sets, and to be used for benchmarking as reference electron densities – are much more difficult to get than 'exact' energies. However, such benchmark studies, even less representative than benchmark studies for energies, would be important for understanding the benefits and drawback of DFT, relative comparisons of various DFT functionals, as well as comparisons of DFT to other quantum chemical methods. A recent study of the performance of various DFT functionals and *ab initio* methods on several atoms and ions revealed possible problems with overfitting of recent DFT functionals on energies.⁸ In Section S2, we expand this comparison of DFT functionals and *ab initio* methods to a large set of molecules and various functional / basis set combinations.

S2. Comparison of the performance of various DFT functionals and *ab initio* methods

S2.1. Comparison to highly accurate *ab initio* results for a few molecules

We have been able to compute $\rho(\mathbf{r})$ of the first six molecules in the QM9 database (CH₄, NH₃, H₂O, C₂H₂, HCN, CH₂O; for a description of the QM9 database, see Appendix A1) with a high level *ab initio* quantum chemical method (CCSD, without a frozen core approximation) often used as a source of 'exact' wave functions, in a large basis set (cc-pCV5Z; for technical details, see Appendix A2). Rapid increase of the cost of computations with the molecule size for high level *ab initio* quantum chemical methods prevents us from carrying out such computations for more than a few first entries in the QM9 database.

For the same six molecules, we also computed $\rho(\mathbf{r})$ using various combinations of DFT functionals and basis sets. In total, 2643 combinations were screened (excluding combinations for which computations did not converge for more than two molecules); for details, see Appendix A2. For each DFT functional, basis set and molecule, an *L1* measure of the accuracy of the predicted electron density $\rho(\mathbf{r})$ was calculated:

$$L1 = \int d\mathbf{r} |\rho(\mathbf{r}) - \rho_{ref}(\mathbf{r})|, \quad (S4)$$

where $\rho(\mathbf{r})$ is the evaluated electron density, and $\rho_{ref}(\mathbf{r})$ is the reference ('exact', CCSD/cc-pCV5Z) electron density. The combinations of DFT functionals and basis sets were sorted by the average value of *L1* over six molecules. The top of the list is given in Table S1. From the analysis of the list we conclude that:

- combinations of DFT functionals and basis sets with low values of *L1* for some of these six molecules tend to have low values of *L1* for the other molecules, and vice versa;
- the top of the list is dominated by two families of functionals (ω B97X-D⁹ and related,¹⁰ and PBE0^{11,12} and related), and one family of basis sets (pcS sets¹³);

- pcS-3-level basis sets yield values of $L1$ as low as V5Z-level basis sets do; neither a shift to pcS-4-level basis sets, nor augmentation of pcS-3-level basis sets significantly improve $L1$.

Table S1. $L1$ measures of the difference between 3D electron densities predicted by various DFT methods with various basis sets, and ‘exact’ (CCSD/cc-pCV5Z) electron densities [Eq. (S4)]. Data are given for the first six molecules in the QM9 database. Top 20 combinations of functionals and basis sets, in the order of increasing average value of $L1$, are shown. Also, some other functionals are given for comparison, each with the basis set providing the highest average $L1$ value for this functional. Double horizontal lines show that some rows were omitted. DFT functionals are named by the corresponding keywords from Gaussian or Q-Chem, except for PBE0 (Gaussian keyword ‘PBE1PBE’).

DFT functional	basis set	1	2	3	4	5	6	average
ω B97X-D3	pcS-3	0.045	0.041	0.039	0.043	0.035	0.058	0.043
ω B97X-D3	aug-pcS-3	0.045	0.042	0.041	0.043	0.036	0.059	0.044
OHSE2PBE	pcS-3	0.052	0.042	0.040	0.041	0.034	0.071	0.047
PBE0	pcS-3	0.058	0.043	0.039	0.039	0.034	0.071	0.047
OHSE2PBE	aug-pcS-3	0.052	0.043	0.041	0.041	0.034	0.071	0.047
ω B97X-D3	cc-pV5Z	0.049	0.040	0.035	0.053	0.044	0.064	0.048
PBE0	aug-pcS-3	0.058	0.044	0.040	0.040	0.034	0.071	0.048
ω B97X-D	pcS-3	0.048	0.047	0.042	0.049	0.039	0.067	0.049
PBEh1PBE	pcS-3	0.057	0.043	0.041	0.043	0.036	0.072	0.049
OHSE1PBE	pcS-3	0.057	0.043	0.041	0.044	0.036	0.073	0.049
HSEH1PBE	pcS-3	0.057	0.043	0.041	0.044	0.036	0.073	0.049
PBEh1PBE	aug-pcS-3	0.057	0.044	0.042	0.043	0.036	0.073	0.049
OHSE1PBE	aug-pcS-3	0.057	0.045	0.042	0.044	0.036	0.073	0.050
HSEH1PBE	aug-pcS-3	0.057	0.045	0.042	0.044	0.036	0.073	0.050
ω B97X-D	aug-pcS-3	0.049	0.048	0.044	0.049	0.040	0.068	0.050
revPBE0	pcS-3	0.050	0.050	0.045	0.041	0.041	0.072	0.050
ω B97X-D3	pcS-4	0.048	0.046	0.045	0.051	0.044	0.065	0.050
ω B97X-D3	aug-pcS-4	0.049	0.046	0.045	0.051	0.045	0.065	0.050
revPBE0	aug-pcS-3	0.051	0.051	0.046	0.042	0.041	0.073	0.051
ω B97X-D3	pc-4	0.049	0.046	0.046	0.053	0.046	0.066	0.051
ω B97X-V	pcS-3	0.048	0.045	0.047	0.058	0.052	0.062	0.052
APFD	cc-pV5Z	0.058	0.040	0.037	0.053	0.046	0.081	0.053
B3PW91	pcS-3	0.055	0.050	0.049	0.052	0.044	0.085	0.056
ω B97X	pcS-3	0.053	0.049	0.049	0.063	0.055	0.071	0.057
mPW3PBE	cc-pV5Z	0.064	0.047	0.044	0.066	0.057	0.093	0.062
TPSSh	pcS-3	0.063	0.066	0.064	0.051	0.051	0.086	0.064
M062X	Apr-cc-pVQZ	0.082	0.062	0.047	0.079	0.072	0.092	0.072
B3LYP	pcS-3	0.093	0.093	0.087	0.117	0.102	0.127	0.103

These results on the accuracy of various DFT methods in predicting $\rho(\mathbf{r})$ cannot be considered as a benchmark study because of a small number of included molecules, which is a consequence of the use of a high-level *ab initio* method and a large basis set to compute the reference (‘exact’) electron densities. However, our major conclusions agree with some other results and theoretical considerations in the literature. In particular, a recent study compared the performance of several DFT functionals in predicting $\rho(\mathbf{r})$ of 30 organic molecules with two to ten heavy atoms (only aug-cc-pVTZ basis set was used). The best method was found to be TPSSh, with PBE0 being only slightly worse.¹⁴ Another study compared the performance of numerous DFT functionals over a set of 14 atoms and monoatomic ions, with a different than $L1$ measure of the accuracy in predicting $\rho(\mathbf{r})$. PBE0 was found to be one of the most accurate DFT methods.⁸ As for the pcS family basis sets, they are rarely included into comparisons, but when they are, they usually perform well.¹⁵⁻¹⁷ Finally, there are some theoretical considerations supporting that ω B97X, PBE0 and related functionals and pcS basis sets may be good at predicting $\rho(\mathbf{r})$ of diverse sets of molecules. PBE0 functional is based to a significant degree on exact theoretical results on the energy functional, not fitting to experimental data.^{8,11,12} ω B97X and related functionals include a relatively small number of fitted parameters.⁶ pcS basis sets, unlike most other basis set families, were designed to fit experimentally measured nuclear magnetic shielding constants, not energies,¹³ which may be the reason for their good performance in approximating $\rho(\mathbf{r})$.

We also carried out similar computations with Hartree-Fock (HF), MP2 and CCSD methods, in combinations with various basis sets, for the same first six molecules in the QM9 dataset (Table S2). As expected, in large basis sets the performance of these *ab initio* methods, in terms of average $L1$ values, is as follows: CCSD < MP2 < HF (from the most accurate to the least accurate method).

Table S2. $L1$ measures of the difference between 3D electron densities predicted by two main *ab initio* methods (MP2 and CCSD) with various basis sets, and ‘exact’ (CCSD/cc-pCV5Z) electron densities [Eq. (S4)]. Data are given for the first six molecules in the QM9 database. Several top basis sets are given for each theory level, in the order of increasing average value of $L1$; the values for HF in a large basis set are also shown for comparison. Double horizontal lines between CCSD/cc-pVQZ and CCSD/pcJ-2 shows that some basis sets with intermediate average $L1$ were omitted. “nan”: computations not converged.

method	basis set	1	2	3	4	5	6	average
MP2	cc-pVQZ	0.044	0.055	0.053	0.069	0.080	0.078	0.063
MP2	cc-pCVQZ	0.045	0.055	0.054	0.071	0.083	0.079	0.064
MP2	def2-QZVP	0.044	0.061	0.064	0.069	0.079	0.081	0.066
MP2	pcS-3	0.043	0.060	0.061	0.075	0.083	0.081	0.067
MP2	aug-cc-pVQZ	0.047	0.064	0.068	0.071	0.079	0.083	0.069
MP2	pc-3	0.044	0.062	0.063	0.078	0.086	0.084	0.069
MP2	pcJ-3	0.045	0.061	0.063	0.078	0.086	0.083	0.069
MP2	aug-cc-pCVQZ	0.048	0.065	0.069	0.073	0.082	0.084	0.070
MP2	pcseg-3	0.046	0.063	0.063	0.078	0.085	0.087	0.070
CCSD	pcJ-3	0.012	0.016	0.017	0.015	0.015	0.018	0.015
CCSD	pcS-3	0.011	0.017	0.018	0.017	0.017	0.019	0.016
CCSD	pc-3	0.013	0.018	0.019	nan	0.020	0.023	0.019
CCSD	def2-QZVP	0.015	0.020	0.021	0.017	0.017	0.022	0.019
CCSD	aug-pcS-3	0.022	0.018	0.019	nan	0.017	0.020	0.019

CCSD	def2-QZVPD	nan	0.020	0.021	0.017	0.017	0.022	0.020
CCSD	aug-pc-3	nan	0.018	0.021	0.020	0.020	0.023	0.020
CCSD	aug-cc-pCVQZ	nan	0.022	0.025	nan	nan	0.026	0.024
CCSD	aug-cc-pVQZ	nan	0.024	0.027	0.022	0.023	0.030	0.025
CCSD	cc-pCVQZ	0.017	0.040	0.037	0.020	0.020	0.029	0.027
CCSD	cc-pVQZ	0.019	0.042	0.039	0.024	0.023	0.032	0.030
CCSD	pcJ-2	0.034	0.044	0.049	0.038	0.043	0.056	0.044
CCSD	aug-cc-pCVTZ	0.043	0.051	0.058	0.052	0.057	0.072	0.055
CCSD	aug-cc-pVTZ	0.046	0.053	0.061	0.054	0.061	0.076	0.058
HF	cc-pCV5Z	0.109	0.114	0.122	0.243	0.238	0.241	0.178

It is particularly interesting to compare the performance of different DFT functionals with *ab initio* methods. DFT methods from the top of the list in Table S1, such as ω B97X-D3 and PBE0, have slightly lower average $L1$ values (~ 0.05) than MP2 with large basis sets (~ 0.06) for the six molecules under consideration, though the ratio of $L1$ for different molecules differ (e.g., for methane MP2 works better than the mentioned DFT functionals). However, many popular DFT functionals, including B3LYP and TPSSh ($L1 \sim 0.06-0.10$), are outperformed (in terms of the $L1$ measure) by MP2 in large basis sets. The performance of CCSD with pcS-3- or VQZ-level basis sets for these six molecules ($L1 \sim 0.01-0.03$) is consistently better than that of DFT, but the use of smaller (VTZ- or pcS-2-level) basis sets kills this advantage of CCSD ($L1 \sim 0.04-0.06$).

Note that the comparisons presented in this Section are limited by the accuracy of the reference electron densities computed with CCSD/cc-pCV5Z. In particular, the reported accuracy of CCSD with smaller basis sets actually reflects the effect of the basis set size, but not the quantum chemical method, on the accuracy of the predicted electron densities. Unfortunately, we have not been able to find in the literature electron densities of these molecules computed with methods of higher level than CCSD, and the widespread quantum chemical software does not allow for computations of electron densities of these molecules with higher level methods either [except for full configuration interaction (FCI), which is implemented in the existing software, but prohibitively expensive with VQZ-level or larger basis sets even for small molecules].

The advantages of the analysis presented in this section are as follows:

- 1) The comparisons are made relative to rather accurate *ab initio* electron densities.
- 2) The molecules for which the comparisons are made contain several types of chemical bonds that are very important as building blocks of larger organic molecules (C–H, N–H, O–H, C=O, C=C, C=N).
- 3) The main conclusions on the relative performance of various *ab initio* and DFT methods are physically sound and match other results in the literature.

However, an evident limitation is that the dataset of six molecules is too small (which is a consequence of using a high-level quantum chemical method and a large basis set). In Section S2.2, we proceed to computations and comparisons for much larger sets of molecules.

S2.2. Comparison to *ab initio* results for larger datasets of molecules

We have been able to compute energies of 4506 molecules from the QM9 dataset (indices 1 to 6000, with omissions) with RI-CCSD(T) method, extrapolated to aug-cc-pVQZ basis set (further denoted as “CCSD(T)/aug-cc-pVQZ” in the quotes; for details on computations, see Appendix A2). The choice of the method was based on the following considerations. CCSD(T), often called ‘a golden standard of Quantum Chemistry’, demonstrates the performance superior to any DFT functional (given a sufficiently large basis set), and it often used as a source of ‘exact’ energies in benchmark studies on various DFT functionals and other quantum chemical methods. Resolution-of-identity [RI in “RI-CCSD(T)”] is a physically motivated approximation within the CCSD(T) framework, which radically improves scaling of the method (thus making it affordable for larger molecules) at a cost of minor errors introduced in the computed energies (at least an order of magnitude smaller than errors of the best DFT functionals, see below). Estimation of RI-CCSD(T)/aug-cc-pVQZ energies by extrapolation from RI-CCSD(T)/aug-cc-pVTZ, RI-MP2/aug-cc-pVQZ and RI-MP2/aug-cc-pVTZ energies further increases the number of molecules from the QM9 dataset for which the computations of energies are affordable. As for the choice of the basis set, aug-cc-pVQZ is the largest one for which an auxiliary basis set required for RI computations was implemented in standard quantum chemical software and used in the literature. Overall, both approximations (RI and extrapolation to aug-cc-pVQZ) are known in the literature to be accurate. The dataset of “CCSD(T)/aug-cc-pVQZ” energies created in this work is, to the best of our knowledge, one of the largest datasets of accurate reference energies, both in terms of the number of molecules and their size (some of the molecules have 8 heavy atoms).

The pairs of DFT functionals and basis sets, providing the lowest errors in computed energies of these 4506 molecules, are given in Table S3. The analysis of these results shows the following:

- M06-2X consistently demonstrates low errors with various basis sets (including triple zeta – level sets).
- ω B97M-V, ω B97X (and, lower on the list, other ω B97* functionals) also have relatively low errors with multiple basis sets.
- The lowest error is demonstrated by ω B97M-V/pcJ-1. The ω B97M-V functional was previously reported as one of the best functionals.⁶ However, it is surprising that the best result is achieved with a small and relatively exotic basis set (pcJ-1) optimized for computations of NMR parameters, not energies. Using larger basis sets from the same family increases the errors in energies (MedAE, kcal/mol: 1.76 for pcJ-1, 2.76 for pcJ-2, 3.02 for pcJ-3). Also, widely used basis sets have errors significantly larger than that of pcJ-1 (MedAE, kcal/mol: 2.80 for aug-cc-pVTZ, 2.84 for aug-cc-pVQZ). It is not clear to us what could be the reasons for ω B97M-V/pcJ-1, but not ω B97M-V with larger basis sets, to stay consistently accurate for such a large and diverse set of molecules.
- The widespread practice of comparing DFT functionals (and, more generally, other quantum chemical methods) for a single basis set may keep important aspects uncovered. In particular, increases in energy errors for larger basis sets may signal that certain functionals might be not as physical as expected from a single smaller basis set comparisons.

Table S3. DFT functionals and basis sets with the lowest errors in predicted energies of 4506 molecules from the QM9 dataset (indices 1 to 6000, with omissions). “CCSD(T)/aug-cc-pVQZ” energies were used as reference (‘exact’) energies. MedAE, median absolute error; MAE, mean absolute error; RMSE, root mean squared error; all errors in *kcal/mol*. The list was sorted by decreasing MedAE to make it more robust to outlying datapoints; MAE values closely correlate with MedAE values.

DFT functional	Basis set	MedAE	MAE	RMSE
ω B97M-V	pcJ-1	1.76	2.11	2.74
M06-2X	def2-TZVPPD	2.02	2.43	3.12
M06-2X	def2-TZVPP	2.10	2.55	3.29
M06-2X	G3LARGE	2.13	2.65	3.43
M06-2X	pcseg-3	2.32	2.80	3.56
M06-2X	cc-pCVQZ	2.33	2.81	3.58
M06-2X	G3MP2LARGE	2.36	2.90	3.73
ω B97M-V	def2-QZVPP	2.37	2.76	3.53
M06-2X	Apr-cc-pVQZ	2.37	2.91	7.16
M06-2X	TApr-cc-pVQZ	2.37	2.91	7.16
ω B97X	aug-pcseg-2	2.38	2.97	7.51
ω B97X	pcseg-2	2.40	2.80	3.57
M06-2X	spAug-cc-pVQZ	2.40	2.96	7.19
M06-2X	aug-cc-pCVQZ	2.41	2.92	3.72

We have also computed electron densities of 52 molecules from the QM9 dataset (indices 1 to 100, with omissions) with RI-CCSD method and aug-cc-pVQZ basis set. As discussed in Section S2.1, only CCSD (not MP2), and only with VQZ-level (not VTZ-level) basis sets provide consistently higher accuracy than DFT methods for the first six molecules in the QM9 dataset. The third order correction in CCSD(T) is defined only for energies, not electron densities. The RI speed up is applicable to CCSD, and we used it to increase the number of molecules for which we could run computations. Basis set extrapolations (e.g., from VTZ-level to VQZ-level basis sets) are reliable and widely used for energies, but not for electron densities. Altogether, these considerations limit our choice of the method to RI-CCSD/aug-cc-pVQZ, and these computations were affordable for 52 molecules. We have not been able to find any previous literature on comparisons of electron densities from high theory level methods for molecules of a size comparable to the largest of these 52 molecules. However, the stability of the relative difference between electron densities from various methods with the molecule size (Fig. 3a) suggests that the relative accuracy of these methods, including RI-CCSD, should stay more or less the same for larger molecules. Combinations of DFT functionals and basis sets with lowest errors in the electron densities (in terms of average *L1* measures relative to RI-CCSD/aug-cc-pVQZ electron densities of 52 molecules) are listed in Table S4.

The analysis of the results on the accuracy of the electron densities computed with various DFT functionals and basis sets shows the following:

- As in the case of the first six molecules (Table S1), the top of the list is dominated by two families of DFT functionals (ω B97X-related and PBE-related), which, as discussed above, are based on exact physical results and/or were designed to minimize possible overfitting.

- pcS-3-level basis sets are often optimal or close to optimal for various DFT functionals (a comparison to V5Z-level or pcS-4-level basis sets, unlike the case of the first six molecules as in Table S1, is not always possible, because computations in larger basis sets are prohibitively expensive for some of these 52 molecules; however, in cases when a comparison is possible, V5Z- and pcS-4-level basis sets do not provide a clear improvement over pcS-3-level basis sets).
- DFT functionals and basis sets with low errors in energies (Table S3) turn out to have relatively large errors in electron densities. In particular, the combination of ω B97M-V/pcJ-1 that worked the best at predicting energies (Table S3) has the median and average $L1$ in electron densities as large as 0.432 and 0.409, respectively, nearly 4 times worse than the best method/basis set combination in Table S4. Also, the M06-2X functional that provided low errors with energies with several basis sets (Table S3) worked worse than many other DFT functionals at predicting the electron densities (the lowest $L1$ were achieved for M06-2X with the cc-pVQZ basis set: median 0.178, average 0.167, which is ~ 1.5 times worse than for ω B97X-D3/pcS-3 or ω B97X-V/pcS-3).

Table S4. DFT functionals and basis sets with the lowest errors in predicted electron densities of 52 molecules from the QM9 dataset (indices 1 to 93, with omissions). RI-CCSD(T)/aug-cc-pVQZ electron densities were used as reference ('exact') densities. The list was sorted by decreasing median $L1$ measures for the electron densities over 52 molecules; average $L1$ measures are also given. Median values closely correlate with average values.

DFT functional	Basis set	Median $L1$	Average $L1$
ω B97X-D3	pcS-3	0.121	0.120
ω B97X-D3	aug-pcS-3	0.121	0.120
ω B97X-V	pcS-3	0.123	0.111
ω B97X-D3	aug-cc-pV5Z	0.125	0.116
ω B97X-D3	cc-pV5Z	0.130	0.129
ω B97X-D3	pcS-4	0.133	0.130
revPBE0	pcS-3	0.135	0.135
ω B97X-D3	pc-4	0.135	0.133
revPBE0	aug-pcS-3	0.136	0.136
ω B97X-D	pcS-3	0.138	0.138
ω B97X-D	aug-pcS-3	0.139	0.139
OHSE2PBE	aug-pcS-3	0.142	0.144

A further comparison of the performance of various DFT functional / basis set combinations at predicting energies and electron densities is given in Fig. S1. From the Hohenberg–Kohn theorems, one would expect that lower errors in electron densities should lead to lower errors in energies, and vice versa, and therefore the dots on the plot should be scattered near a line (or a curve) with a positive slope (Fig. S1, *green dotted line*). Instead, we observe a relatively independent scattering in terms of these two types of errors, with a negative slope of the convex hull of the dots in the region of low errors. Thus, for the best existing DFT functionals, lower errors in energies are associated with higher errors in electron densities and vice versa, which does not seem to agree with the trend predicted by the Hohenberg–Kohn theorems, which is a sign of overfitting the existing functionals to energy predictions. As seen from Fig. S1, realistic error levels achievable with the best existing DFT functionals

found by “human learning” are on the order of ~ 3 kcal/mol for energies and ~ 0.1 for the $L1$ measure for electron densities.

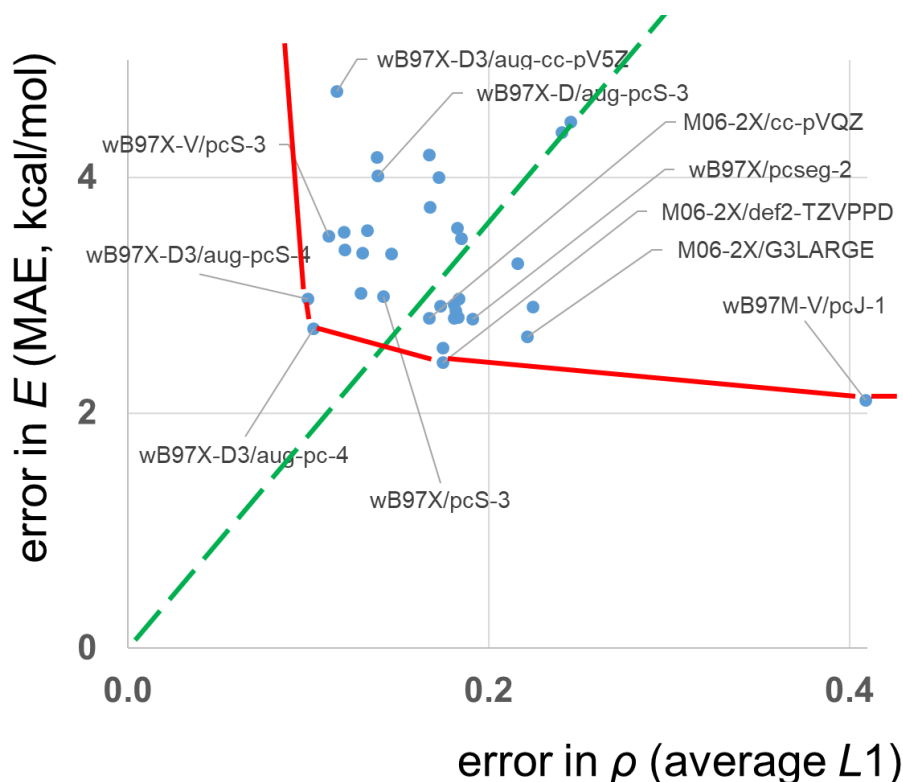


Fig. S1. DFT functionals and basis sets best at predicting energies work worse at predicting electron densities, and vice versa. Errors in energies (MAE, kcal/mol) are plotted against errors in electron densities (average $L1$ measure) for multiple combinations of DFT functionals and basis sets (*blue dots*). From the Hohenberg–Kohn theorems, one would expect lower errors in energies to be associated with lower errors in electron densities (*green*), but in practice we observe a relatively independent distribution of errors, with the convex hull (*red*) having a negative slope. These empirical data suggest that DFT functionals previously built by “human learning” may be overfitted to the specific task of energy predictions.

S2.3. Choice of the method / basis set pairs to generate data for ML

A rapid increase of the cost of computations with the molecule size necessitates two-stage training of the neural network: first, on a larger dataset generated with a computationally cheaper (and hence less accurate) method / basis set combination, and second, on a dataset of more accurate (and hence more scarce) results.

For the first stage, our choice of the method and basis set was based on two considerations: (1) computations should be fast enough to treat $\sim 133,000$ molecules in a reasonable amount of time (up to several months), given the computational resources we had, and (2) the accuracy of the computed electron densities and energies should be higher than that achievable with other methods and basis sets of comparable computational cost.

For 176 combinations of DFT functionals and basis sets that provided the lowest average values of $L1$ for the first six molecules (Section S2.1), we ran a standard quantum chemical software for three larger molecules (QM9 entries 8 000, 16 000 and 32 000). (Here we use the data on the accuracy for the first six molecules, because we

chose the DFT method and basis set for large-scale computations for the whole QM9 dataset long before we carried out the analysis presented in Section S2.2.) Then, we computed an aggregated indicator showing how much wallclock time is required to run DFT computations for a molecule of this size on a single GPU (further called ‘effective time’; for exact definition and computation details, see Appendix A2). The plot for the computational cost (estimated by effective time) vs. accuracy in predicting $\rho(\mathbf{r})$ (estimated by average $L1$ over the first six QM9 molecules) shows that some combinations of a DFT functional and a basis set have a favorable tradeoff between the cost and accuracy in predicting $\rho(\mathbf{r})$ (Fig. S2). PBE0/pcS-3, which is #4 on the list in Table S1, looks particularly attractive. Other good choices might be PBE1hPBE/pcS-3, PBE0/Def2-QZVP, and possibly ω B97X-D/cc-pV5Z (though the last combination is more expensive). As for the first three combinations on the list in Table S1, computations for ω B97X-D3¹⁰ with pcS-3-level basis sets turned out to be prohibitively expensive to run them for the whole QM9 dataset, while OHSE2PBE (also known as HSE03) is less used in the literature than PBE0, and its gain in accuracy over PBE0/pcS-3 is marginal.

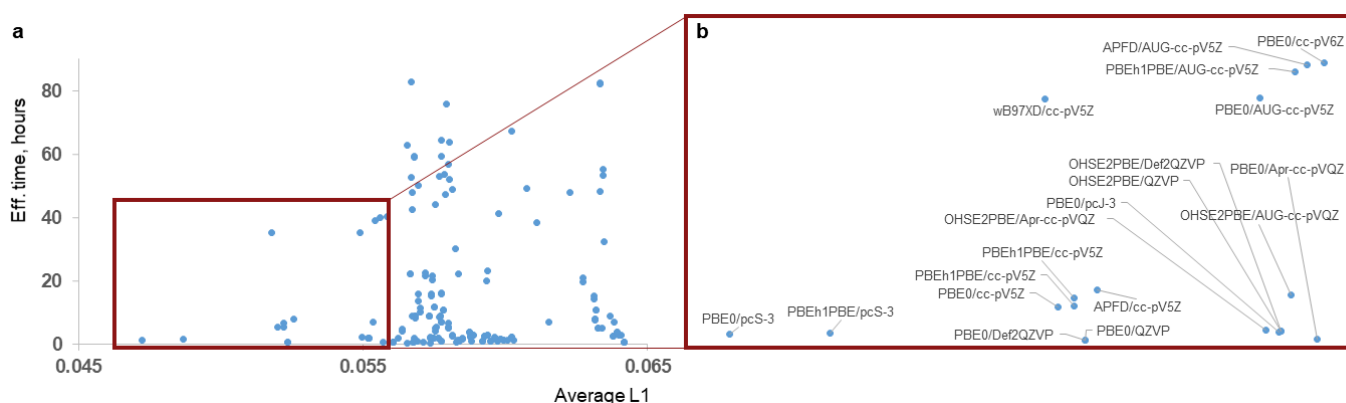


Fig. S2. Comparison of accuracy in predicting electron densities (measured by $L1$ averaged over first six molecules from the QM9 database) vs. computation cost (estimated by ‘effective time’, based on wallclock time for running computations for QM9 entries 8 000, 16 000 and 32 000, see Appendix A2) for various combinations of DFT functionals and basis sets. Attractive options are PBE0/pcS-3 (which is #4 on the list in Table S1), PBE1hPBE/pcS-3, PBE0/Def2-QZVP, and possibly ω B97X-D/cc-pV5Z. (a) All functional/basis set combinations with average $L1 < 0.065$ shown; (b) combinations with $L1 < 0.056$, with labels.

Based on the provided data, we chose the combination of PBE0 functional and pcS-3 basis set to compute DFT electron densities for molecules in the QM9 dataset to be used at the first stage of training. This combination has a reasonable computational cost (it took us several months to compute electron densities of all molecules in the QM9 dataset with it). It also demonstrated good performance in predictions of electron densities of 52 molecules for which CCSD/aug-cc-pVQZ densities were available (Fig. 3a), though some other combinations were later found to be a bit more accurate (Fig. S6).

Unfortunately, energies predicted with PBE0/pcS-3 turned out to be significantly less accurate than those reported in the QM9 database [computed with B3LYP/6-31G(2df,p)]. In comparison to available 4504 “CCSD(T)/aug-cc-pVQZ” energies, MAE of PBE0/pcS-3 was 10.5 kcal/mol, while that of B3LYP/6-31G(2df,p) energies was 4.6 kcal/mol (median absolute errors: 10.4 and 4.1 kcal/mol, respectively). In order not to repeat computations for all ~133,000 molecules from the QM9 dataset to get energies with another DFT functional and basis set, which would

be time- and resource-consuming, we chose to use B3LYP/6-31G(2df,p) energies reported in the original QM9 dataset for the first stage of ML.

Due to high cost of CCSD computations in large basis sets, especially for molecules like the overwhelming majority of molecules in the QM9 database, it is currently impractical to use such methods to generate datasets of electronic densities comparable in size to QM9. As for smaller basis sets (e.g., VTZ-level sets),^{14,18} from the viewpoint of $L1$ metric of the total electron densities, even the use of CCSD without a frozen core approximation does not offer an increase in performance in comparison to much faster and better scaling DFT methods, such as PBE0. The same refers to MP2 methods, regardless of the used basis set: in the best case scenario, they can offer only a marginal improvement in $L1$ values, not worth the increase in the computational cost (MP2 calculations are more expensive than those with PBE0).

We would like to emphasize that we do not claim here that a certain DFT functional or a basis sets is “the best”. Different research goals (and hence, metrics of performance, not only the $L1$ and MedAE measures used in this work) and different availability of computational resources may make different choices of quantum chemical methods and basis sets optimal under different circumstances.

As for the second stage of ML, we used RI-CCSD/aug-cc-pVQZ electron densities and “CCSD(T)/aug-cc-pVQZ” energies for the reasons discussed above in Section S2.2. To briefly recap, CCSD and CCSD(T) (but not MP2) methods guarantee significantly higher accuracy than DFT for electron densities and energies, respectively, and this higher accuracy can be achieved only with VQZ-level (but not VTZ-level) basis sets. aug-cc-pVQZ is the largest VQZ-level basis set for which auxiliary basis sets required for RI speed up is available in popular quantum chemical packages.

S3. Derivation of the main equations in this work

S3.1. Corrections derived from Taylor series

For the exact Hohenberg-Kohn density functional $E[\rho]$ of the electron density $\rho(\mathbf{r})$, the Taylor series expansion (up to the second order) in the vicinity of some density $\rho_0(\mathbf{r})$ close to the ground state density can be written as:

$$E[\rho_0 + \Delta\rho] \cong E[\rho_0] + \int d\mathbf{r} \left(\frac{\delta E}{\delta \rho(\mathbf{r})} \right)_{\rho_0} \Delta\rho(\mathbf{r}) + \frac{1}{2} \int d\mathbf{r} d\mathbf{r}' \left(\frac{\delta^2 E}{\delta \rho(\mathbf{r}) \delta \rho(\mathbf{r}')} \right)_{\rho_0} \Delta\rho(\mathbf{r}) \Delta\rho(\mathbf{r}'), \quad (\text{S5})$$

where $\Delta\rho(\mathbf{r}) = \rho(\mathbf{r}) - \rho_0(\mathbf{r})$, and $\delta E/\delta \rho(\mathbf{r})$ and $\delta^2 E/\delta \rho(\mathbf{r}) \delta \rho(\mathbf{r}')$ are the first- and second-order functional derivatives of the density functional $E[\cdot]$, respectively. The minimum of $E[\rho_0 + \Delta\rho]$ under the constraint that

$$\int d\mathbf{r} \Delta\rho(\mathbf{r}) = 0 \quad (\text{S6})$$

(which maintains a constant number of electrons in the molecule) is reached at the following values of $\Delta\rho$ and ΔE :

$$\Delta\rho(\mathbf{r}) = - \int d\mathbf{r}' \left(\frac{\delta^2 E}{\delta\rho(\mathbf{r})\delta\rho(\mathbf{r}')} \right)_{\rho_0}^{-1} \left[\left(\frac{\delta E}{\delta\rho(\mathbf{r}')} \right) - \Delta\mu \right]_{\rho_0}, \quad (\text{S7})$$

$$\Delta E = -\frac{1}{2} \int d\mathbf{r}d\mathbf{r}' \left[\left(\frac{\delta E}{\delta\rho(\mathbf{r}')} \right) - \Delta\mu \right]_{\rho_0} \left(\frac{\delta^2 E}{\delta\rho(\mathbf{r})\delta\rho(\mathbf{r}')} \right)_{\rho_0}^{-1} \left[\left(\frac{\delta E}{\delta\rho(\mathbf{r}')} \right) - \Delta\mu \right]_{\rho_0}, \quad (\text{S8})$$

where $\Delta\mu$ is a Lagrange multiplier ensuring the electron number conservation, the value of which is implicitly set by Eqs. (S6) and (S7), $(\delta^2 E/\delta\rho(\mathbf{r})\delta\rho(\mathbf{r}'))^{-1}$ is the resolvent for the second-order functional derivative of the density functional, and ΔE is defined as $E[\rho_0 + \Delta\rho] - E[\rho_0]$. Thus, $\Delta\rho$ and ΔE can be considered as corrections to the approximate electron density ρ_0 and energy $E[\rho_0]$, respectively.

Though these expressions for $\Delta\rho$ and ΔE were derived from the second order Taylor series, Eq. (S5), they can be further generalized to include higher order functional derivatives. For example, a perturbative inclusion of the third order functional derivative $\delta^3 E/\delta\rho(\mathbf{r})\delta\rho(\mathbf{r}')\delta\rho(\mathbf{r}'')$ leads to the following expression for $\Delta\rho$:

$$\begin{aligned} \Delta\rho(\mathbf{r}) = & - \int d\mathbf{r}' \left(\frac{\delta^2 E}{\delta\rho(\mathbf{r})\delta\rho(\mathbf{r}')} \right)_{\rho_0}^{-1} \left[\left(\frac{\delta E}{\delta\rho(\mathbf{r}')} \right) - \Delta\mu \right]_{\rho_0} \\ & + \frac{1}{2} \int d\mathbf{r}'d\mathbf{r}'' \left(\frac{\delta^3 E}{\delta\rho(\mathbf{r})\delta\rho(\mathbf{r}')\delta\rho(\mathbf{r}'')} \right)_{\rho_0} \Delta\rho_{l_0}(\mathbf{r}')\Delta\rho_{l_0}(\mathbf{r}'') \Big|_{\rho_0}, \end{aligned} \quad (\text{S9})$$

where

$$\Delta\rho_{l_0}(\mathbf{r}) = - \int d\mathbf{r}' \left(\frac{\delta^2 E}{\delta\rho(\mathbf{r})\delta\rho(\mathbf{r}')} \right)_{\rho_0}^{-1} \left[\left(\frac{\delta E}{\delta\rho(\mathbf{r}')} \right) - \Delta\mu \right]_{\rho_0}. \quad (\text{S10})$$

The idea of this generalization is illustrated in more detail in Appendix A3 for a simple case of a function of one variable. Overall, if functional derivatives of $E[\rho]$ of all orders exist, then an exact series expansion for $\Delta\rho$ (and hence for ΔE) can be written in terms of the values of these functional derivatives at ρ_0 , in a way similar to Eq. (S9). These series for $\Delta\rho$ and ΔE can be interpreted as values of two new functionals evaluated at ρ_0 . Denoting these functionals as $\Delta\rho[\cdot]$ and $\Delta E[\cdot]$, respectively, we arrive at the fundamental result of this work:

$$\Delta\rho(\mathbf{r}) = \Delta\rho[\rho_0], \quad (\text{S11})$$

$$\Delta E = \Delta E[\rho_0] \quad (\text{S12})$$

(strictly speaking, only $\Delta E[\cdot]$ is a functional, that is a function-to-number mapping, while $\Delta\rho[\cdot]$ is a function-to-function mapping). Here, $\Delta\rho[\cdot]$ and $\Delta E[\cdot]$ are uniquely defined by $E[\cdot]$. Note that Eqs. (S11)-(S12), unlike Eqs. (S7)-(S8), are exact (not limited to the second order Taylor series expansion) due to including higher order terms [such as the third order term in Eq. (S9)].

Thus, the corrections to the electron density and energy can be computed as the values of $\Delta\rho[\cdot]$ and $\Delta E[\cdot]$ at ρ_0 , avoiding the computationally expensive procedure of iterative minimization of $E[\rho]$. Moreover, ML can be directly applied to learn $\Delta\rho[\cdot]$ and $\Delta E[\cdot]$, without any need to learn $E[\cdot]$. The forking architecture of the DNN

proposed in the main text is justified by the fact that the expressions for $\Delta\rho$ and ΔE in Eqs. (S7)-(S9) are built of similar blocks, and therefore, can be computed from a shared set of intermediate results.

To the best of our knowledge, the existence of all higher order functional derivatives of the density functional $E[\cdot]$ has not been strictly proven in DFT yet, though, on the other hand, no symptoms of their non-existence have been reported either. If only a limited number of higher order functional derivatives of $E[\cdot]$ exists, then the equations like Eqs. (S7)-(S8), and therefore Eqs. (S11)-(S12), can be used as approximations. In practice, this should not limit the approach proposed in this work, as soon as the reference electron density ρ_0 is close to the exact one, because mappings $\Delta\rho[\cdot]$ and $\Delta E[\cdot]$ are in any case supposed to be found by ML, therefore, only approximately.

S3.2. Choice of the reference electron density ρ_0

So far, we have not imposed any restrictions on ρ_0 in Eq. (S5), besides that it should be somewhat close to the true ground state electron density of the simulated molecule. However, in the interests of practical efficiency, a more specific choice of ρ_0 can be made. Indeed, the function-to-function mapping $\Delta\rho[\cdot]$ introduced in Section S3.1, in general, has to be very sensitive to the input. Regardless of whether $\rho_0(\mathbf{r})$ or $\rho_0(\mathbf{r}) + \delta\rho(\mathbf{r})$, where $\delta\rho(\mathbf{r})$ is an arbitrary function, is used as the reference density, the predicted values of $\rho(\mathbf{r})$ should be the same:

$$\rho(\mathbf{r}) = \rho_0(\mathbf{r}) + \Delta\rho[\rho_0(\mathbf{r})] = [\rho_0(\mathbf{r}) + \delta\rho(\mathbf{r})] + \Delta\rho[\rho_0(\mathbf{r}) + \delta\rho(\mathbf{r})], \quad (\text{S13})$$

and therefore,

$$\Delta\rho[\rho_0(\mathbf{r}) + \delta\rho(\mathbf{r})] = \Delta\rho[\rho_0(\mathbf{r})] - \delta\rho(\mathbf{r}). \quad (\text{S14})$$

It would be very difficult to ensure this property of $\Delta\rho[\cdot]$ without using an overcomplicated DNN and a very large training set. Instead, a simple prescription on the choice of ρ_0 can ensure that Eq. (S14) is automatically satisfied.

We start from the fact that relatively good analytical approximations to the exact density functional $E[\rho]$ are provided by HF or existing versions of DFT (at least, some of them; see Section S2). For a specific approximate density functional $E^{(0)}[\rho]$ previously found by ‘‘human learning’’, the exact functional $E[\rho]$ can be written as

$$E[\rho] = E^{(0)}[\rho] + E^{(1)}[\rho], \quad (\text{S15})$$

where $E^{(1)}[\rho]$ is the correction to the density functional defined by this equation, Eq. (S15). Then, the correction to the electron density $\Delta\rho$ can be split into two contributions, matching the splitting of $E[\cdot]$ in Eq. (S15), namely:

$$\Delta\rho = \Delta\rho^{(0)} + \Delta\rho^{(1)}, \quad (\text{S16})$$

where the first term is the difference between the *exact* solution for the *approximate* density functional $E^{(0)}[\cdot]$ and the reference density ρ_0 :

$$\Delta\rho^{(0)} = \underset{n(\mathbf{r})}{\operatorname{argmin}} E^{(0)}[n(\mathbf{r})] - \rho_0(\mathbf{r}), \quad (\text{S17})$$

and the second term is the difference between the exact solutions for $E[\cdot]$ and $E^{(0)}[\cdot]$:

$$\Delta\rho^{(1)} = \underset{n(\mathbf{r})}{\operatorname{argmin}} E[n(\mathbf{r})] - \underset{n(\mathbf{r})}{\operatorname{argmin}} E^{(0)}[n(\mathbf{r})]. \quad (\text{S18})$$

In these notations, the exact electron density $\rho(\mathbf{r})$ can be written in the following form:

$$\rho(\mathbf{r}) = \rho_0(\mathbf{r}) + \Delta\rho^{(0)}[\rho_0(\mathbf{r})] + \Delta\rho^{(1)}[\rho_0(\mathbf{r}) + \Delta\rho^{(0)}[\rho_0(\mathbf{r})]]. \quad (\text{S19})$$

With this equation, the condition given by Eq. (S14) is automatically satisfied (Fig. S3). Since the correction $\Delta\rho^{(0)}$ depends only on the known functional $E^{(0)}[\cdot]$, it can be found analytically or numerically with the traditional methods and existing software. Only the second correction, $\Delta\rho^{(1)}$, needs to be learned with ML, and the corresponding function-to-function mapping is pretty robust in the sense that it does not need to be as sensitive to the input as $\Delta\rho$ [Eq. (S14)].

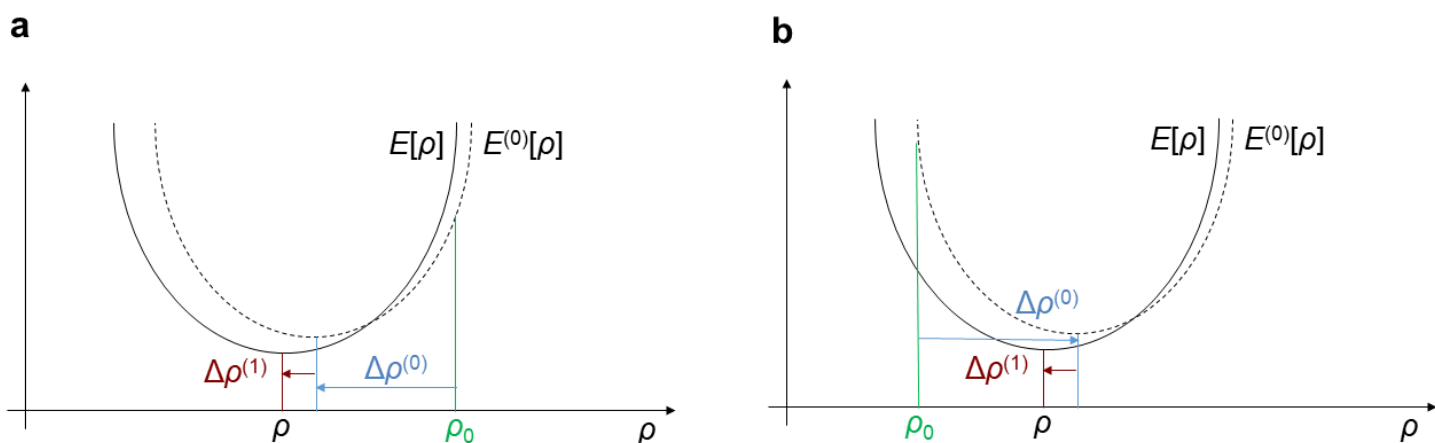


Fig. S3. A schematic illustration of Eq. (S19) in two dimensions. (In fact, $\rho(\mathbf{r})$ and $\rho_0(\mathbf{r})$ are functions, and $E[\rho]$ and $E^{(0)}[\rho]$ are functionals.) (a) To go from an approximate electron density ρ_0 (green) to the exact density ρ that minimizes $E[\rho]$, we first go to the minimum of $E^{(0)}[\rho]$ (blue), and after that to the minimum of $E[\rho]$ (cardinal). (b) If we start from another approximate electron density ρ_0 (green), the first step is different (blue), but the second step is the same (cardinal). This splitting of $\Delta\rho$ into $\Delta\rho^{(0)}$ and $\Delta\rho^{(1)}$ ensures the robustness of the mapping to be approximated with ML ($\Delta\rho^{(1)}$ only, cardinal).

If ρ_0 is chosen to be the electron density that minimizes $E^{(0)}[\rho]$, in other words, is **the solution for a given molecule provided by a specific version of DFT (or HF, which can also be formulated in the form of a density functional minimization¹⁹)**, then $\Delta\rho^{(0)}(\mathbf{r})$ vanishes, and Eq. (S19) simplifies to

$$\rho(\mathbf{r}) = \rho_0(\mathbf{r}) + \Delta\rho^{(1)}[\rho_0(\mathbf{r})], \quad (\text{S20})$$

where $\Delta\rho^{(1)}(\mathbf{r})$ is supposed to be learned with ML. This equation, together with the corresponding equation for the exact energy E , is given in the main text of the paper (with the notational simplification that $\Delta\rho^{(1)} = \Delta\rho$, valid in the case of the choice of ρ_0 as the solution provided by a specific DFT or HF method, which is assumed in the main text). Without the restriction that ρ_0 is a solution from HF or a specific DFT method, we would not have been able to use Eq. (S20); instead, a more general and more computationally expensive Eq. (S19) would have to be used.

S4. DNN architecture and training

S4.1. Input and output format

The only **input** to the reported DNN is an approximate electron density of a molecule of interest computed with HF method ρ_{HF} . Preparation of an input file is carried out in three steps:

- (1) For a given molecule, HF calculations are run in standard quantum mechanical software.
- (2) Using the fchk file generated in step (1), a cube file for the total electron density is generated. This cube file contains numerical values of the electron density on $256 \times 256 \times 256$ grid points with a grid spacing of 0.1 bohr ($\sim 0.05 \text{ \AA}$). This grid spacing is necessary to approximate integrals over the volume, as in Eq. (S4), by summation over grid points. The number of grid points in each direction was chosen following a tradition in the field of deep learning to use power-of-two grids, which simplifies architectures of neural networks (a $128 \times 128 \times 128$ grid with a grid spacing of 0.1 bohr is not large enough to contain some of the largest QM9 molecules).
- (3) The $256 \times 256 \times 256$ cube file generated in step (2) is coarse grained to a $64 \times 64 \times 64$ cube file by summation of the electron density values in non-overlapping $4 \times 4 \times 4$ cubes. We perform this transformation to speed up DNN training, and make training possible on a single GPU. We checked that this coarse-graining quantitatively preserves the spatial behavior of the electron density. Coarse-graining of a $256 \times 256 \times 256$ cube into a $64 \times 64 \times 64$ cube ensures that the integral of the electron density computed from a sum of the values on all grid points has the right value, and mitigates artifacts of discrete representation of the electron density near nuclei where the gradient of the density is large. A $64 \times 64 \times 64$ cube file with a grid spacing of 0.4 bohr directly generated from the fchk file does not satisfy either of these two conditions, hence the need for separate steps (2) and (3).

The immediate **output** from the DNN is $\Delta\rho$, which is the difference between ρ and ρ_{HF} :

$$\Delta\rho(\mathbf{r}) = \rho(\mathbf{r}) - \rho_{\text{HF}}(\mathbf{r}), \quad (\text{S21})$$

and $\Delta E'$, defined as:

$$\Delta E' = \left(E - \sum_{a \in H,C,N,O,F} E_a n_a \right) - \left(E_{\text{HF}} - \sum_{a \in H,C,N,O,F} E_{\text{HF},a} n_a \right) - \left[c_0 + \sum_{a \in H,C,N,O,F} c_a n_a \right], \quad (\text{S22})$$

where E_a is the energy of an isolated atom a computed with the same quantum chemical method as the energy of the molecule E , n_a is the number of atoms of element a in the molecule, E_{HF} and $E_{\text{HF},a}$ are energies of the molecule and of an isolated atom a , respectively, computed with the HF method in the cc-pVDZ basis set, and c_0 and c_a are empirical coefficients found from the least square fit of the equation

$$\left(E - \sum_{a \in H,C,N,O,F} E_a n_a \right) - \left(E_{\text{HF}} - \sum_{a \in H,C,N,O,F} E_{\text{HF},a} n_a \right) \approx c_0 + \sum_{a \in H,C,N,O,F} c_a n_a, \quad (\text{S23})$$

over the molecules in the training set ($c_0 = 0.002720$, $c_H = -0.020721$, $c_C = -0.076106$, $c_N = -0.108908$, $c_O = -0.087452$, $c_F = -0.058814$, all values in hartree). The use of the linear correction term in Eq. (S22) allows us to increase the accuracy of the model, because the DNN focuses in this case on finding relatively small, but

complicated contributions to the energy of chemical binding, and not larger, but conceptually simple corrections per atom. In other words, the DNN is used to predict the discrepancies, Eq. (S22), between the right and left hand sides of Eq. (S23). Note that this approach does not contradict to the general theory presented in Section 3. Comparing this definition of $\Delta E'$ to ΔE from the main text, one can see that

$$\Delta E' = \Delta E - \left[c_0 + \sum_{a \in H, C, N, O, F} (E_a - E_{HF,a} + c_a) n_a \right], \quad (\text{S24})$$

which is also a functional of $\rho_{HF}(\mathbf{r})$, because numbers of atoms of each type in a given molecule can be found from an approximate electron density,

$$n_a = n_a[\rho_{HF}(\mathbf{r})], \quad (\text{S25})$$

and all other entities inside the square brackets in Eq. (S24) are constants. Thus, $\Delta E'$ can be considered as a functional of ρ_{HF} , like ΔE .

From $\Delta\rho$, the desired values of ρ can be easily computed, because ρ_{HF} is already known. The values of $\Delta\rho$ used for training were computed from PBE0/pcS-3 results similar to ρ_{HF} as described above, and represented after coarse-graining in the form of $64 \times 64 \times 64$ cube files. The output of the DNN follows the same format of $\Delta\rho$ representation. Similarly, the value of $\Delta E'$ predicted by the DNN is sufficient to compute the desired value of E , because E_{HF} is known from the HF/cc-VDZ computation that we perform anyway to get the input to the DNN, and the linear correction term is easy to compute from the molecular formula.

S4.2. Architecture

The architecture of the DNN is shown in Fig. 1d in the main text. The only input channel is the HF/cc-VDZ density given on a $64 \times 64 \times 64$ grid. First, this input is processed elementwise with a tanh function [namely, $\tanh(1.28\rho_{HF})$], such that ρ_{HF} in the regions where $\rho_{HF} \gtrsim 0.8$ (typical of atomic cores) saturates to 1, while in other regions (including covalent bonds and regions responsible for non-covalent interactions) the input is only linearly rescaled. This transformation ensures that the information on chemical bonding is not dwarfed by the atomic core densities, and artifacts of a discrete representation of the density near the atomic cores are removed. Next, the information is processed by ten hidden layers with a U-Net architecture. This type of architecture was originally proposed to process medical images,²⁰ and proved efficient in other physics-related tasks.²¹ The first five hidden layers encode step-by-step the input into a very coarse spatial representation, the subsequent five hidden layers decode it back to the original resolution, and there is also a direct flow of information from encoding hidden layers to decoding hidden layers having the same spatial resolution (hence the term ‘U-Net’ for the architecture). Along this path, spatial resolution goes from $64 \times 64 \times 64$ to $2 \times 2 \times 2$ and then back to $64 \times 64 \times 64$, and intermediate representations include up to 256 channels. At the end of the U-Net block, a tensor with 64 channels, each of which has a $64 \times 64 \times 64$ spatial resolution, is computed and concatenated with the input (after tanh transformation), yielding a 65-channel tensor. After this concatenation, computations fork into two paths – one for the electron density and the other for the energy calculations. The density is computed by a convolution of the concatenated tensor to 32 channels with the same spatial resolution, rectified linear unit (ReLU) activation, and convolution of the result to a single channel yielding the predicted $\Delta\rho$ values on a $64 \times 64 \times 64$ grid. The other

path of computations includes two subsequent 3D convolution operations, each of which is followed by ReLu activation, such that the first convolution decreases the number of channels to 32, and the second convolution to two. Finally, the output value of ΔE is computed as a linear function of the elements in these two channels and on all $64 \times 64 \times 64$ grid points. This forked architecture of the network is designed to push the model to learn first some general high-level features of molecules, such as the first-order functional derivative of the density functional, or the resolvent for the second-order derivative (Fig. 1b-d), and only after than to employ these general features to solve the specific tasks of computing the energy or electron density of a given molecule.

S4.3. Loss functions and training curves

The loss function L to be minimized to train the PML-QC_{DFT} model was chosen as a linear combination of the $L1$ measures of the performance of the DNN in predicting the electron densities and energies, with an additional regularization term:

$$L = \sum_{i \in \text{training set}} \|\Delta\rho_{DNN}[\rho_{HF,i}(\mathbf{r})] - \Delta\rho_i(\mathbf{r})\| + w_E \sum_{i \in \text{training set}} |\Delta E'_{DNN}[\rho_{HF,i}(\mathbf{r})] - \Delta E'_i| + w_{Ereg} \sum_{j \in K} k_j^2, \quad (\text{S26})$$

where i numerates molecules in the training set, $\Delta\rho_i(\mathbf{r})$ and $\Delta E'_i$ are the ground truth (i.e., computed from DFT for training the PML-QC_{DFT} model) values of $\Delta\rho$ and $\Delta E'$ [Eqs. (S21) and (S24)] for the i -th molecule, $\rho_{HF,i}(\mathbf{r})$ is the input (HF/cc-VDZ) electron density for the i -th molecule, $\Delta\rho_{DNN}$ and $\Delta E'_{DNN}$ are the values of $\Delta\rho(\mathbf{r})$ and $\Delta E'$ predicted by the DNN for the i -th molecule, w_E is a coefficient defining a relative weight of the electron density and energy discrepancies in the overall estimate of the performance of the DNN, w_{Ereg} is a prefactor for the regularization term, K is the set of kernel coefficients in convolution operations within the path to the energy prediction from the bifurcation, j enumerates these coefficients, and k_j are the values of these coefficients. No regularization for the kernel coefficients from the path to the electron density predictions was included in L , because we did not observe any significant overfitting for $\Delta\rho$ predictions. The matrix $L1$ norm in the loss function in Eq. (S26) is interpreted as follows:

$$\|a(\mathbf{r})\| = \int d\mathbf{r} |a(\mathbf{r})|, \quad (\text{S27})$$

which is estimated numerically by summation of $|a(\mathbf{r})|$ over all points on the $64 \times 64 \times 64$ grid.

To train the PML-QC_{DFT} model, we split the QM9 database into training, validation and testing subsets based on the following rules. All molecules with 9 heavy atoms (QM9 indices 21989 to 133885) and indices matching the mask “???[2-9]??”, where “[2-9]” stands for any digit from 2 to 9, were assigned to the training set. All molecules with 9 heavy atoms and indices “???1??” were assigned to the validation set, and all molecules with 9 heavy atoms and indices “???0??” were assigned to test set 1. Finally, all molecules with 1 to 8 heavy atoms (indices up to 21988) were considered as a separate test set 2. This approach allows us to test the transferability of the PML-QC_{DFT} model between atoms with different numbers of heavy atoms (9 vs. 1 to 8), and to compare predictions of the PML-QC_{DFT} to high quantum theory level results in large basis sets (available for molecules with a few atoms) for molecules not included in the training set. In this way, 89,432 molecules (66.8% of the whole QM9 dataset) were assigned to the training set, 11,191 molecules (8.4%) to the validation set, 11,194 molecules (8.4%) to test

set 1, and 21963 molecules (16.4%) to test set 2. Besides that, 55 molecules originally present in the QM9 database (0.04%) were excluded because PBE0/pcS-3 computations for them did not converge, and 50 more molecules (0.04%) were excluded because DFT results for them did not seem reliable (specifically, two different functional / basis set combinations – PBE0/pcS-3 and B3LYP/6-31G(2df,p) – led to $\Delta E'$ values that differed by more than 50 kcal/mol).

The PML-QC_{DFT} model was trained in four stages. First, w_E and w_{Ereg} were set to 0, the learning rate was set to $2 \cdot 10^{-4}$, and 12 epochs of training were performed. During each epoch, all molecules in the training set, randomly sorted, were processed in minibatches of 16 molecules, such that each molecule was used once and only once during each epoch. Second, w_E was changed to 10^4 , and 12 more epochs of training were performed, with w_{Ereg} equal to $d_{Ereg}i_{Epoch}$ at each epoch, where i_{Epoch} increased from 1 to 12, and the value of d_{Ereg} optimal for the regularization was found to be 10 (Fig. S4). Third, 12 more epochs were carried out with the learning rate of $2 \cdot 10^{-5}$, and w_{Ereg} equal to $d_{Ereg}i_{Epoch}$, where i_{Epoch} ran from 13 to 24. Finally, one more epoch was carried out, with the learning rate of $2 \cdot 10^{-6}$, and $w_{Ereg} = d_{Ereg}i_{Epoch}$, where $i_{Epoch} = 25$. The value of $w_E = 10^4$ was chosen such that the contribution of the energy term to the total loss function L , Eq. (S26), was $\sim 10\%$ of L by the end of training (as measured on the validation set). An attempt to significantly increase w_E did not lead to noticeable changes in the performance of the trained model in terms of ΔE or $\Delta\rho$ prediction. Attempts to use other training schedules, including ones with a gradual decrease in the learning rate and a gradual increase in w_E and w_{Ereg} values throughout training epochs, did not yield better models (data not shown).

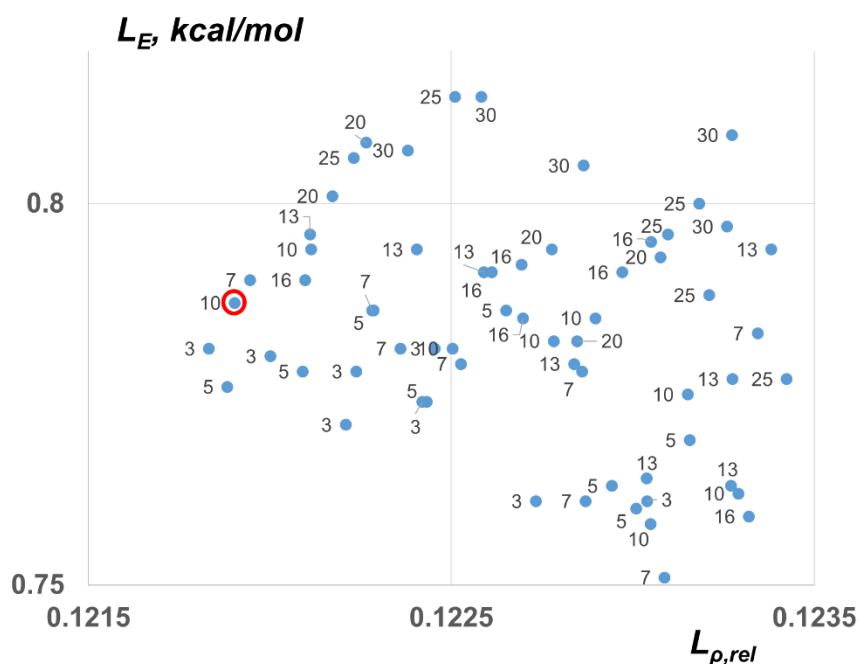


Fig. S4. Optimal value of d_{Ereg} for the network regularization was chosen by comparing the performance (on the validation set) of models trained with different d_{Ereg} values. Final L_{ρ} vs. L_E values over the validation set for each independent training session shown, with the corresponding values of d_{Ereg} used as labels. Multiple independent training sessions were run for each d_{Ereg} . Models trained with $d_{Ereg} > 10$ demonstrated deteriorated performance on the validation test set, so we chose $d_{Ereg} = 10$ as the optimal value. One of the models learned with $d_{Ereg} = 10$ was chosen as the final PML-QC_{DFT} model (red circle). This model has the lowest error in predicting densities (among models with $d_{Ereg} = 10$), and a relatively low error in energies.

As for training the PML-QC_{CCSD} model, we had CCSD(T) data on energies only for molecules with QM9 indices up to 6000 (with omissions), and CCSD data on electron densities only for molecules with QM9 indices up to 93 (with omissions). All of these molecules were in test set 2 when we trained the PML-QC_{DFT} model. For this reason, we had to divide the available set of 4504 molecules with known CCSD(T) energies into new training, validation and test sets: 3612 molecules with indices “???[2-9]??” were assigned to the training set, 463 molecules with indices “???1??” to the validation set, and 430 molecules with indices “???0??” to the test set. CCSD electron densities were available only for 52 molecules with QM9 indices up to 93 (with omissions). This dataset was split in the following way: molecules with 3 or 4 heavy atoms (indices 9 to 48, with omissions) were assigned to the training set, and molecules with 1, 2 or 5 heavy atoms (indices 1 to 8 and 49 to 93) to the test set. A validation set for CCSD electron densities was not formed due to the scarcity of the data.

The PML-QC_{CCSD} model reported here was trained in three stages, each of which included 100 epochs. Learning rates during the first, second and the third stages were kept constant and equal to $2 \cdot 10^{-4}$, $1 \cdot 10^{-4}$, and $2 \cdot 10^{-5}$, respectively. Each epoch included 100 sub-epochs of minimization of $\sum_{i \in \text{training set}} \|\Delta \rho_{DNN}[\rho_{HF,i}(\mathbf{r})] - \Delta \rho_i(\mathbf{r})\|$ and 1 sub-epoch of minimization of $\sum_{i \in \text{training set}} |\Delta E'_{DNN}[\rho_{HF,i}(\mathbf{r})] - \Delta E'_i|$ [simultaneous minimization of L defined by Eq. (S26) was impossible, because training sets for the energies and electron densities were different). The proportion of 100 sub-epochs vs. 1 sub-epoch was found empirically, as that ensuring comparable relative rates of decay of the loss functions for the energies and densities. No regularization for the energy term was performed, because there were no noticeable signs of overtraining in terms of energy predictions for the PML-QC_{CCSD} model (unlike the PML-QC_{DFT} model). The parameters to be changed during training were the kernel coefficients in convolution operators in the paths leading to the energy and density predictions, as well as in the last layer before the bifurcation.

To analyze the progress in training, we recorded two variables, measuring the performance of both DNNs in terms of $\Delta \rho$ and ΔE predictions separately from each other. The first variable is the average L_1 measure for the performance of the DNN in predicting $\rho(\mathbf{r})$ of molecules in set S , defined as follows:

$$L_\rho = \frac{1}{\|S\|} \sum_{i \in S} \|\Delta \rho_{DNN}[\rho_{HF,i}(\mathbf{r})] - \Delta \rho_i(\mathbf{r})\|, \quad (\text{S28})$$

which corresponds the first term on the right hand side of Eq. (S26) (S here may stand for training, validation or test sets). The second variable is the mean absolute error in predicted energies L_E , a parameter widely used in the literature on benchmarking in Quantum Chemistry:

$$L_E = \frac{1}{\|S\|} \sum_{i \in S} |\Delta E'_{DNN}[\rho_{HF,i}(\mathbf{r})] - \Delta E'_i|, \quad (\text{S29})$$

where $\|S\|$ is the number of molecules in set S . Evidently, the energy term in the total loss function L , Eq. (S26), is proportional to this MAE.

During training, L_ρ and L_E on the training set, as expected, gradually decreased for both models (Fig. S5). L_ρ and L_E computed on the validation set also tended to decrease. Note that the values of L_ρ and L_E for the validation set were computed at the end of each training epoch (with the enumeration of epochs starting from 1) using the same state of the DNN (after training on all minibatches in the corresponding epoch) and all molecules from the validation set, while the values of L_ρ and L_E for the training set were computed differently: the DNN was updated

after each minibatch, the contributions to L for the molecules in the current minibatch were computed with the current DNN and averaged over all minibatches. Respectively, the values of L_ρ and L_E for the training set are shown in Fig. S5 in the middle between the indices of the previous and next epochs.

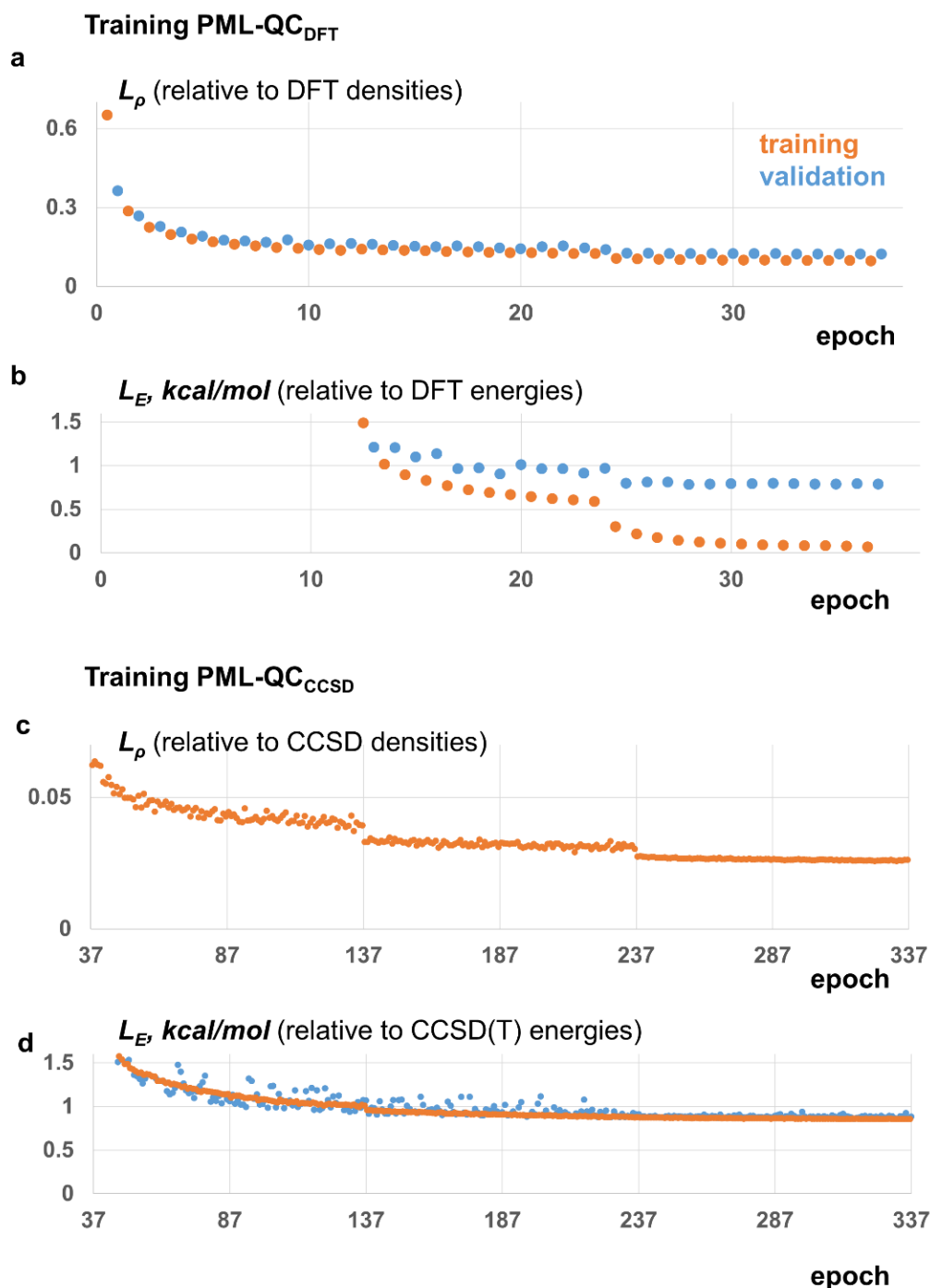


Fig. S5. Learning curves for (a,b) PML-QC_{DFT} and (c,d) PML-QC_{CCSD} models in terms of predictions of electron densities (a,c) and energies (b,d). Validation for the electron densities predicted by PML-QC_{CCSD} was not performed due to a limited number of CCSD electron densities; for comparison of the performance of the model on training and test data for each molecule in the dataset, see Fig. 3a in the main text.

S4.4. Performance of the resulting models on training, validation and test sets

By the end of training of the **PML-QC_{DFT} model**, L_ρ on the validation set decreased to 0.122 and stabilized at this level for 2-4 last training epochs (Fig. S5a). The difference of L_ρ over the training (0.097) and validation (0.122) sets is minor, implying that there is no significant overfitting of the PML-QC_{DFT} model on the electron density data. Over test set 1 (~10% of QM9 molecules with nine heavy atoms), L_ρ was found to be 0.094, confirming the conclusion that there was no overfitting of the model on electron densities. For test set 2 (all molecules with up to eight heavy atoms), L_ρ was found to be somewhat lower, namely 0.086, suggesting that the PML-QC_{DFT} model is transferrable to molecules of sizes different from those in the training set.

L_E for the PML-QC_{DFT} model computed over the validation set decreased to 0.79 kcal/mol by the end of training, staying stable at this level over the last 4-6 training epochs (Fig. S5b). The corresponding value for the training set was much lower, 0.07 kcal/mol, even with the regularization as described above, Eq. (S26). With $d_{Ereg} = 10$, the value of the regularization term per molecule, in energy terms, reached 0.21 kcal/mol by the end of training; larger values of d_{Ereg} only increased the values of L_E over the validation set, and did not reduce the gap between the results on the training and validation sets (data not shown). The performance of the model on test set 1 (~10% of molecules with nine heavy atoms) is close to that for the validation set: L_E 0.82 kcal/mol, while on test set 2 (all molecules with up to eight heavy atoms) L_E was even lower, 0.58 kcal/mol. Median absolute errors were 0.54 and 0.38 kcal/mol for test sets 1 and 2, respectively. Most of the molecules in test set 2 have exactly eight heavy atoms, the mean error per heavy atom is even lower for test set 2 than for test set 1 or the validation set. Therefore, the PML-QC_{DFT} model extrapolates well to molecules with a different number of atoms than in the training set, both in terms of energy and electron density. The value of L_E demonstrated by the PML-QC_{DFT} model is on par with MAE values of other ML models over the QM9 dataset reported in the literature²²⁻³³ (Table S5). As for the performance of the model in terms of electron densities, a comparison to the literature cannot be made, because no models predicting electron densities for datasets as large as QM9, to the best of our knowledge, have been published so far.

The values of L_ρ and L_E given above refer to a comparison of predicted electron densities and energies to DFT values [PBE0/pcS-3 densities and B3LYP/6-31G(2df,p) energies, respectively]. Comparisons to more physical CCSD electron densities (Fig. 3a, *pink*) and CCSD(T) energies (Table 1) demonstrates that the accuracy of the PML-QC_{DFT} model is actually nearly the same as the accuracy of the DFT methods used to generate the training sets.

The performance of the **PML-QC_{CCSD} model** on the datasets with CCSD electron densities and CCSD(T) energies was as follows. The value of L_ρ decreased by the end of training to 0.026 and stayed stable over the last ~30-50 (out of 300) epochs (Fig. S5c). Due to a limited number of molecules for which CCSD electron densities were computed, a comparison of the errors of the PML-QC_{CCSD} model, HF, various DFT and other methods can be visually performed molecule-by-molecule (Fig. 3a, Fig. S6). Though the errors for molecules in the test set are larger than for those in the training set, they stay below the corresponding errors of DFT (Fig. 3a, Fig. S6). The value of L_E by the end of training fell down to 0.86 kcal/mol for the training set and 0.88 kcal/mol for the validation set, staying stable over the last ~30-50 (out of 300) epochs (Fig. S5d). Over the test set, L_E (in other words, MAE) was as low as 0.86 kcal/mol, and the median absolute error was 0.71 kcal/mol.

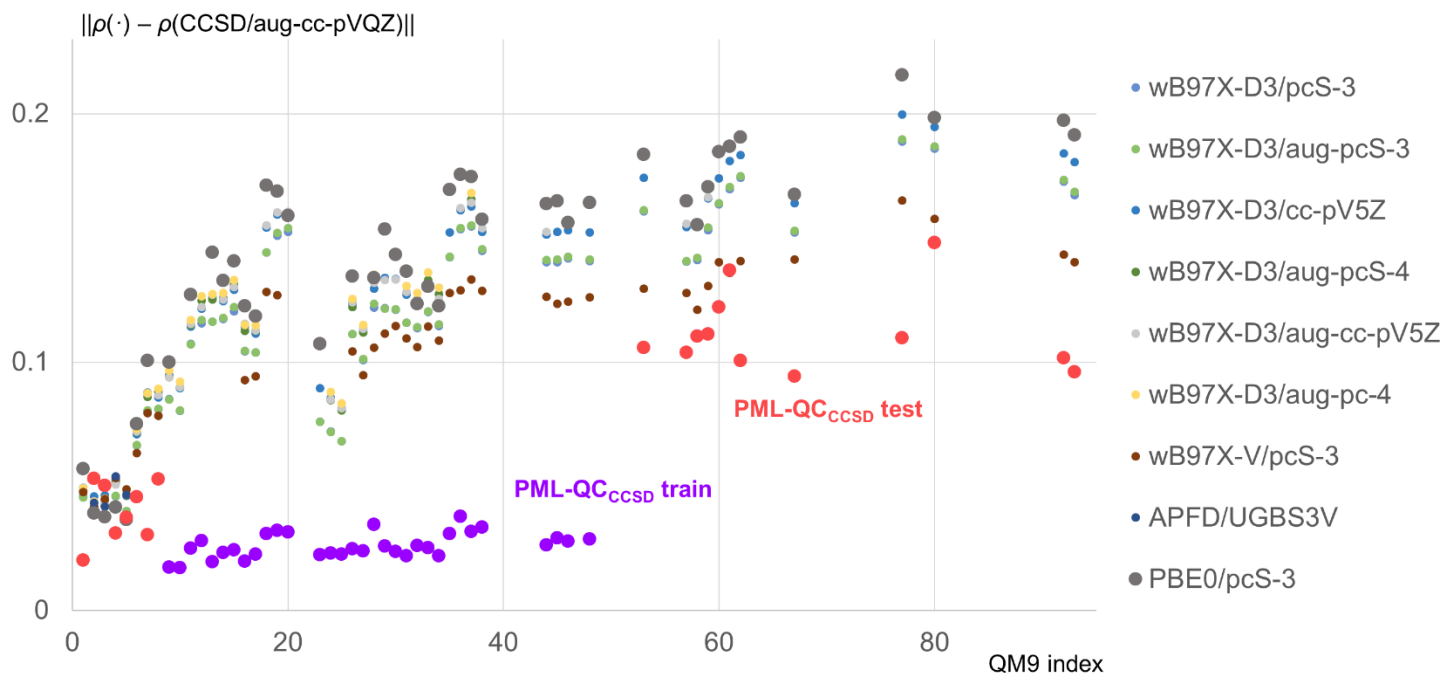


Fig. S6. The PML-QC_{CCSD} model outperforms all DFT methods, not only PBE0/pcS-3, in predicting electron densities of 52 molecules for which we had reference CCSD/aug-cc-pVQZ electron densities. This figure supplements Fig. 3a from the main text. Only combinations of DFT methods and basis sets with the lowest values of L_ρ are shown.

To the best of our knowledge, only one paper so far has compared energies predicted with ML to CCSD(T)-level energies for a large dataset of molecules.³⁴ They reported the MAE of 1.46 kcal/mol for a set of organic molecules with 10 to 13 heavy atoms, i.e. somewhere between $1.46/13 = 0.112$ and $1.46/10 = 0.146$ kcal/mol per heavy atom. In this work, the mean absolute error per heavy atom of the PML-QC_{CCSD} model over the test set (430 molecules, QM9 indices up to 6000, matching the mask“???0??”, with omissions) is 0.146 kcal/mol.

S4.5. Scaling

DNN computations run much faster on the same hardware (1 GPU and 2 CPUs, see Appendix A2 for details) than DFT (PBE0/pcS-3) computations for every molecule in the QM9 dataset (Fig. 2f). For the overwhelming majority of the database entries (with indices ~ 100 and higher) the DNN is at least two orders of magnitude faster than DFT. HF computations in the small basis set, required to generate the DNN input, are also much faster than DFT computations for the same molecules. The bottleneck in the computational pipeline turned out to be the step of generation of input cube files from HF fchk files. To generate cube files, we used cubegen utility from Gaussian, which is currently implemented only on a single CPU. We expect that this stage can be significantly speeded up in the future with parallelization and the use of GPUs. Even in the current setup, the DNN computations, together with HF computations and generation of the input cube files, are faster than DFT (PBE0/pcS-3) computations for all expect the first four molecules in the QM9 database. Closer to the end of the database, the gain in the speed (measured by wallclock time) reaches a factor of ~ 30 . (Only relative wallclock

times are shown in this work; absolute values of wallclock times for computations performed in Gaussian are not disclosed according to the Gaussian licensing agreement.)

Wallclock time to run the reported DNN stays virtually the same over the whole QM9 dataset due to the architecture of the reported DNN. Wallclock time of HF computations increases with the number of electrons N as $\sim N^{1.62}$, while PBE0/pcS-3 wallclock time scales less favorably, as $\sim N^{3.26}$. Due to this difference in scaling of the DNN, HF and DFT cost with the size of the molecule, the relative efficiency of the approach proposed here increases with the size of a modeled molecule. The ratio of the wallclock time for HF to that for DFT is $\sim 10\%$ for the first several molecules in the database (entries 1-6), falls to $\sim 1\%$ by entry ~ 100 , and falls even further to $\sim 0.3\%$ closer to the end of the dataset. The wallclock time for the DNN relative to the wallclock time for DFT falls from $\sim 30\%$ for the first several molecules to $\sim 1\%$ by entry ~ 100 , and down to $\sim 0.1-0.3\%$ by the end of the database. As for the relative price of the HF and DNN parts, the DNN stage dominates for smaller systems with up to ~ 30 electrons. For larger systems, HF becomes consistently more expensive (pronouncedly from ~ 60 electrons), but the gap between the HF and DFT costs in this limit increases. We do not consider here the scaling of wallclock time for the cube file generation, because, as stated earlier, we expect that this part of computations can be significantly accelerated in comparison to the current version.

S5. Additional discussion

Recently, machine learning (ML) – and, more specifically, deep learning, that is ML with deep neural networks (DNNs) – have achieved impressive results in dealing with large sets of data, including three-dimensional shapes and functions.³⁵⁻³⁸ ML is also starting to be actively and fruitfully applied to various problems in Quantum Chemistry (for reviews, see Refs.³⁹⁻⁴³). In particular, DNNs and other ML models were reported to predict energies of molecules (primarily organic) as functions of atomic coordinates with thermochemical accuracy and at much smaller computational cost than quantum chemical methods (ANI-1* potentials and many others).^{18,22-34,44-54} The resulting models demonstrated remarkable performance on various test sets of molecules. For example, a number of architecturally diverse models were reported to reach accuracy levels on the order of 1 kcal/mol for organic molecules in the QM9 database (Table S4).^{22,23,25-33} In these models, the energy is approximated as a function of various descriptors that can be easily computed from the geometry, such as lists of distances to the closest atoms for each atom in the molecule, but do not have a clear quantum mechanical interpretation.^{18,22-28,30-33,41,44-46,49-52}

At the same time, electron densities have been out of focus of ML in this field so far. To the best of our knowledge, ML have been used to predict electron densities only in specific molecular systems, such as sulfur-crosslinked carbon nanotubes,⁴⁶ Ni/Al alloys,⁴⁷ dihydrogen, water, benzene, ethane, and malonaldehyde.⁴⁴ The question of feasibility of electron density learning in wide classes of chemical compounds remains open.

Some papers on the use of ML in Quantum Chemistry take into account the Hohenberg–Kohn theorems² stating the existence of the energy functional of the electron density (Section S1), and trying to approximate this functional (or one of its nontrivial components) with ML methods.^{18,42-44,55-59} However, the use of learned energy functional in an iterative minimization procedure may be computationally expensive than a single-shot computations of the density and energy as suggested in this work. Also, minimization / maximization tasks for DNNs are known to be associated with artifacts, such as "adversarial examples" (slightly perturbed images that

are wrongly classified by DNNs, though the original images were classified correctly).^{60,61} Optimization procedures with functions or functionals approximated by DNNs in Quantum Chemistry may encounter similar problems, ending up in unphysical solutions ("adversarial electron densities"). To circumvent these difficulties, we propose in this work to learn the functional $\Delta E[\cdot]$ and the function-to-function mapping $\Delta\rho[\cdot]$, rather than the Hohenberg-Kohn functional $E[\cdot]$.

Electron density prediction is not only an important physical problem *per se*. In the neural networks we report in this work, computations fork into two paths – one for the energy and the other for the electron density calculations – much closer to the end of the network, thereby pushing the model to learn first some general high-level characteristics, and only after that to employ them to solve the specific tasks of computing the energy or electron density of a given molecule. By including the electron densities into the loss function to be minimized during DNN training, we additionally regularize the model, make it more physical and more resistant to overfitting to a specific task of predicting energies. Though some ML models in the literature were trained to predict properties dependent on electron densities, such as partial charges, dipole moments, etc.,^{14,25,26,31,48,62,63} and therefore may also be regularized by these additional predictions, the use of electron densities should work better due to richer information contained in them. Besides that, in order to ensure regularization, predictions of such properties and energies should be done from a shared pool of highly processed features, and will not happen if such predictions are performed by independent neural networks, as often done in the literature.

A promising direction in ML in Quantum Chemistry is to generate features for ML by a simple-and-fast quantum chemical method, and then to use neural networks to predict results of high-level methods in large basis sets. In this way, it was suggested to use HF matrix elements (but not the electron densities or SCF solutions) to predict MP2 and CCSD energies,⁶⁴ or to use MP2 amplitudes to predict coupled cluster energies.⁶⁵ Such approaches are computationally more expensive at the stage of featurization, in comparison to using descriptors easily computed from the molecular geometry, but latest advances in speeding up HF computations should mitigate this issue. However, previous papers on the use of HF (or other low-theory-level) computations to featurize a molecule do not clarify the question of what entities computed with these methods can serve as features, and why they do so. In this paper, we demonstrate that it is an approximate (e.g., HF) electron density that can serve as a universal way to featurize a molecule (Section S3).

The DNN we report predicted multiple features in the density differences, even though the input densities did not contain anything similar to such features. For example, toroidal parts of isosurfaces around C–C and C–H bonds (Fig. 2c and Movie S2, $\Delta\rho = -0.003$) have been placed by the PML-QC_{DFT} model in correct positions, perpendicular to the corresponding chemical bonds, and at a distance where the input density is small by absolute value and does not include any toroidal formations. Also, the DNN learned to distinguish all heavy atoms (C, N, O, F), as seen from correct density difference isosurfaces predicted around them (correspond to 0, 1, 2 and 3 lone pairs, respectively), though no information on the chemical nature of these atoms or their nuclear charges has been explicitly passed to the neural network.

In all cases of significant discrepancies between the PML-QC_{DFT} predictions and DFT results, we found that errors were in the scale of $\Delta\rho_{\text{DNN}}$, but not its local spatial behavior. This might be corrected in future work by adding an additional layer to be learned to perform a nonlinear transformation of the output density, or simply by adding more hidden layers to the network to allow for more flexible nonlinear fitting (though this would slow down computations).

As for predicting energies, the reported models reached the accuracy levels below 1 kcal/mol [the PML-QC_{DFT} model: in comparison to DFT energies, and the PML-QC_{DFT} model: in comparison to CCSD(T) energies], which is on par with models reported in the literature (Table S5). Note that nearly all papers compare ML predictions to DFT-level energies (e.g., those included in the QM9 database), which, as we showed in Section S2, may be away from the exact energies by several kcal/mol. The only comparison of ML to CCSD(T) energies for a large set of molecules, as far as we know, was reported in ref. 34. The MAE value from that work (1.46 kcal/mol) is not directly comparable to the MAE value for the PML-QC_{CCSD} model reported in this work (0.86 kcal/mol): the former value refers to 2996 molecules with 10 to 13 C, N and O atoms and conformations with energies within 100 kcal/mol of minima, while the latter value refers to ~2000 molecules with 1 to 8 (in most cases, 7) C, N, O and F atoms and conformations close to the energy minima. However, MAE values per heavy atoms seem comparable in two cases (0.146 kcal/mol for the PML-QC_{CCSD} model, and somewhere between $1.46/13 = 0.112$ and $1.46/10 = 0.146$ kcal/mol for the cited paper). Note, however, that the PML-QC_{CCSD} model we report predicts not only energies, but also electron densities.

Table S5. Mean average errors (MAE) of some recent ML models on QM9 or datasets of similar sizes.

Reference	Benchmark	Year	MAE, kcal/mol	Comment
<i>Comparison to DFT-level energies</i>				
22	QM9	2017	0.58	Kernel ridge regression (with HDAD descriptors), trained on ~ 118 000 molecules, tested on the remaining molecules
23,32	QM9	2017	0.31	Continuous-filter convolutional neural network SchNet (with 6 interaction blocks), trained on 110 462 molecules
24	QM9	2017	0.84	Deep tensor neural network (with 3 interaction passes), trained on 100 000 molecules
45	ANI-1	2017	0.78	Deep neural network ANI, trained on ~14 mln. datapoints (equilibrium and non-equilibrium conformations) for ~56 000 molecules from GDB-8 database. For maximal comparability with the other data in this table, MAE computed on minimum energy conformations of 134 random molecules from GDB-10 database is provided (from Table S3 in the cited paper)
25	QM9	2018	3.05	Kernel ridge regression model (variant $12^{NP}3^B$), trained on the first 3 993 molecules from QM9, MAE computed over the whole QM9
26	QM9	2018	0.30	Kernel ridge regression-based model, trained on 20 000 molecules and tested on 2 000 molecules
27	QM9	2018	1.83	High-dimensional neural network potentials HDNNPs (with wACSF descriptors), trained (and cross-validated) on 10 000 molecules, tested on ~ 123 000 molecules
28	QM9	2018	0.41	Moment tensor model, trained on 50 000 molecules
29	QM9	2018	2.64	Combination of semiempirical density functional tight-binding method with ML of generalized pair-potentials (with 259 bond

				types), trained on 2 100 molecules (supplemented with their non-equilibrium conformations), and tested on ~ 130 000 molecules
30	QM9	2018	0.26	Hierarchically interacting particle neural network (with 80 atomic features per layer), trained and tested on ~ 131 000 molecules
31	QM9	2018	1.5	Kernel ridge regression (with $F_{2B} + F_{3B}$ features), trained on 5 000 random molecules and tested on 126 722 molecules
33	QM9	2018	0.41	Neural networks with two hidden square unit augmented layers, trained on 100 000 molecules and tested on ~ 31 000 molecules
53	GDB07to09	2018	0.80	Deep neural network ANI-1x, trained on 25% of ANI-1 database with active learning. For maximal comparability with the other data in this table, MAE computed on GDB07to09 benchmark (1500 molecules with 7, 8 or 9 C, N, O atoms) for conformations with energy within 10 kcal/mol of minima are provided (from Table S15 in the cited paper)
This work	QM9	2019	0.78	PML-QC _{DFT} : Deep neural network, trained on 89 432 molecules, validated on 11 191 molecules, and tested on 11 194 and 21 963 molecules (test sets 1 and 2)
Comparison to CCSD(T)-level energies				
34	CCSD(T)*/CBS	2019	1.46	Deep neural network ANI-1ccx, obtained from ANI-1x by transfer learning on CCSD(T)* energy data. MAE computed on GDB10to13 benchmark (2996 molecules with 10 to 13 C, N, O atoms) for conformations with energy within 100 kcal/mol of minima is provided (from Table 1 in the cited paper).
This work	“CCSD(T)/aug-cc-pVQZ” (Section S2.2)	2019	0.86	PML-QC _{CCSD} ; DNN retrained on 3612 energies, and tested on 430 energies

Due to the chosen architecture of the DNN, the cost of the DNN computations stays nearly constant as a function of the size of a molecule (Fig. 2f). However, this relationship holds only for molecules that fit into the cube grid we used in this work. In general, for molecules much larger than those in the QM9 database, larger grids would be required, and a new DNN with a different architecture would have to be trained. We speculate that the cost of DNN predictions in this regime will scale in the range between $\sim N \log N$ and $\sim N^3 \log N$, depending on the shape of molecules. The first factor (N to N^3) comes from an increase of the required 3D grid size: for compact molecules, roughly linearly with the molecule volume, hence roughly linearly with N , but for elongated molecules, roughly cubically with the molecule length, hence cubically with N . The second factor, $\log N$, estimates possible increase in the depth of the network that may be required to process larger grids. The scaling could be made more favorable (maybe down to $\sim N \log N$) with more flexible designs of DNNs, enabling them to work with non-cubic inputs of variable size, e.g., scanning window architectures. This would allow for $\sim N$, not $\sim N^3$, scaling of the input size for elongated molecules. However, such an optimization of DNNs might not be a top priority now, because for large molecular systems, which are of more practical interest, HF computations are more expensive than DNN computations (Fig. 2f).

Speaking of possible practical applications of DNNs capable of predicting electron densities, first of all, we note that the knowledge of the electron density is sufficient to compute forces acting on all atoms in a molecular system, as follows from the Hellmann-Feynman theorem. We expect that these computations will be more accurate than computations based on direct fits for energies as functions of the molecular geometries, because the former approach involves integration, while the latter involves differentiation of approximate functions. Along this way, one may be able to run *ab initio* molecular dynamics simulations accounting for the correlation energy at a low computational cost. Besides calculations of forces, electron densities predicted by DNNs can be used to study inter- and intramolecular interactions, and to compute any quantum mechanical observables that depend only on one-particle electron density, including dipole and higher-order electric moments of molecules.

It is important to emphasize that ML does not replace or invalidate the methods of Quantum Chemistry. In fact, ML reinforces these methods and extends them to a wider realm of practical applicability. Unlike *ab initio* methods, predictions of electron densities and energies with DNN are expected to have much more favorable scaling, as discussed above. However, this favorable scaling can be achieved only on the basis of running high-level quantum chemical computations for molecules in a sufficiently large training database. The use of DNNs therefore separates the problem of increasing the accuracy of quantum chemical methods from the problem of routine applicability of such methods. With ML, it may become not required that an accurate quantum chemical method works fast enough for every new molecule that an end user may be interested in. Instead, the focus shifts to generating highly accurate results only for a finite dataset to be used for training, while the efficiency in practical applications is to be achieved via improvements in DNNs to make them faster and more accurate.

In connection to the problem of training datasets, a question that still remains open is how the performance of various quantum chemical methods, in combinations with various basis sets, relates to each other. This question is very important from the practical viewpoint, because it determines the strategy of generating datasets for ML. Which theory level and basis set to use, given limited computational resources? In this work, we generated the database of DFT (PBE0/pcS-3) solutions for the QM9 dataset, and RI-CCSD/aug-cc-pVQZ densities and "CCSD(T)/aug-cc-pVQZ" energies for a subset of QM9. However, these electron densities and energies are still not equal to the exact ones, as follows from Table S1 and S2. What will be the next level of accuracy for QM9 or other quantum mechanical databases of a similar size? This question is of major practical importance, and answering it may require running large-scale benchmark computations for various methods and basis sets.

Other possible directions for further research include the following. Databases of electron densities for a large number of inorganic molecules, organic molecules with more elements than in QM9, ions, noncovalently bound molecular complexes and other molecular systems not included in the QM9 database should be built and used for validation of the proposed approach of physical machine learning. New architectures of DNNs, allowing for piecewise scanning of input and output, could be developed to remove a restriction on the size of a modeled system that exists in the reported DNN. Also, the present approach needs to be extended to modeling geometries of molecules far from equilibrium, processes of bond formation and breaking, and excited electronic states.

We would like to end this discussion by recapping that the key element of success in applications of ML in Quantum Chemistry, in our opinion, lies in involving as much physics as possible into ML models. We demonstrate in this work that the use of HF (or DFT) electron densities, even computed in a small basis set, looks promising, presumably because such a representation is more physical than other descriptors. Training ML models not only on energies, but also on electron densities may serve as a possible strategy to make models more physical, and stimulate learning the physics of modeled phenomena, rather than curve fitting.

APPENDICES

A1. Brief characterization of the QM9 dataset

Out of several quantum chemical databases of molecules, we chose to work with QM9.⁶⁶ This database includes 133,885 organic molecules made up of C, H, N, O and F elements. All molecules in QM9 have up to nine heavy (non-hydrogen) atoms, zero electric charge, and zero spin. The QM9 database includes the geometries of all molecules optimized with B3LYP DFT functional and 6-31G(2df,p) basis set. Unlike other existing quantum chemical databases,^{45,67-69} QM9 is at the same time easy to work with (all data files can be easily downloaded and processed locally); contains more molecules than most other databases, but still a manageable number of molecules to run quantum chemical computations for all of them with our resources; includes F (not only C, H, N, O), and focuses on conformations close to equilibrium (we chose to investigate how to do ML of electron densities in molecules near equilibrium before proceeding to non-equilibrium geometries, because it can be seen from the existing literature that the problem of building a neural network applicable to multiple molecules is much more difficult than the problem of building a network predicting energies of thermally sampled non-equilibrium geometries of one or several molecules). In this work, we make the results of our quantum chemical computations for the QM9 dataset available to all researchers by publishing it in a public repository, hoping that these data on the wavefunctions and electron densities of more than 133 thousand molecules will foster further progress in the field of ML in Quantum Chemistry.

A2. Quantum chemical computations

Production DFT (**PBE0/pcS-3**) computations for all molecules in the QM9 database were carried out in Gaussian 16, revision A.03 (Gaussian, Inc.). Each computation used one GPU (NVIDIA Kepler GK210, in NVIDIA Tesla K80) and two CPUs (in Intel Xeon CPU E5-2680 v2) on XStream, a Cray CS-Storm GPU compute cluster at Stanford University (<http://xstream.stanford.edu>). The geometry of all molecules was taken from the QM9 database. No changes in the geometry, such as energy minimization, were made. Computations in Gaussian were run with DFT functional “PBE1PBE” and keywords “NoSymmetry Output=WFX Density=Current Population=Full”. The pcS-3 basis set was downloaded from EMSL Basis Set Library (<https://bse.pnl.gov>).^{70,71} Both wfx and chk files were recorded; fchk files were subsequently generated from chk files with formchk utility from Gaussian. Cube files for the total electron density were generated from fchk files with cubegen utility from Gaussian with keyword “FDensity=SCF”. The grid had 256 points per each side (cubic $256 \times 256 \times 256$ grid), and the step size of 0.1 bohr in each direction. Each molecule was positioned in the middle of a cube (i.e., shifted in space relative to the position in the original QM9 database); no rotations of the molecules were performed. The resulting $256 \times 256 \times 256$ cube files were coarse-grained to $64 \times 64 \times 64$ cube files using a simple C++ code written by us.

Production **HF/cc-pVDZ** computations for all molecules in the QM9 database were carried out in the same way as PBE0/pcS-3 computations (see above), except that the method keyword was “HF”, and the cc-pVDZ basis set internally implemented in Gaussian was used.

Reference **CCSD/cc-pCV5Z** computations for the first six molecules from the QM9 database were carried out in Gaussian (as above). Each computation used one CPU (in Intel Xeon E5-4640, E5-4650v4 or E5-2697Av4) and up to 400 GB of memory on Sherlock, a high-performance computing cluster at Stanford University (<https://www.sherlock.stanford.edu>). To make the full use of the symmetry of these small molecules, Z-matrices accounting for their high symmetry were manually generated. The values of the bond lengths, angles and dihedral angles were computed from the corresponding Cartesian coordinates in the QM9 database; in the cases of small differences between such values computed from different subsets of atoms related by symmetry operations, arithmetic averages of the values were used. No other changes in the geometry, such as energy minimization, were performed. The basis set was taken from EMSL Basis Set Library (as above). Keywords “Output=WFX Density=Current Population=Full” were used. Both wfx and chk files were recorded; fchk files were subsequently generated from chk files with formchk utility from Gaussian. Cube files for the total electron density were generated from fchk files with cubegen utility from Gaussian with keyword “FDensity=CC”. The grid had 161 points per each side (cubic $161 \times 161 \times 161$ grid), and the step size of 0.1 bohr in each direction. No shifts or rotations of the molecules in the cube files were performed (due to the use of Z-matrices rather than coordinates from the QM9 database for these computations).

Various **HF, MP2, CCSD and DFT computations with various basis sets** for the purpose of generating data shown in Tables S1 and S2 were carried out in Gaussian (as above) or Q-Chem, version 5.1.0 (Q-Chem, Inc.). Computations were run on XStream (as above) with the use of one CPU and one GPU (as above), or on Sherlock (as above) with the use of one CPU (as above). Z-matrices, the same as in CCSD/cc-pCV5Z computations, were used. Basis sets internally implemented in Gaussian or Q-Chem were used. For computations in Gaussian, chk files were saved, converted to fchk files, and then cube files ($161 \times 161 \times 161$ grid, step size of 0.1 bohr) were computed (as above). For computations in Q-Chem, cube files of the same size were directly generated, with the use of “make_cube_files true” keyword in the Q-Chem input files. No frozen cores were used in any of these computations.

The following DFT functionals were screened (keywords for the methods in the corresponding software are given): APFD, B3LYP, B3PW91, BLYP, HSEH1PBE, M062X, mPW3PBE, OHSE1PBE, OHSE2PBE, PBE1PBE, PBEh1PBE, TPSSh, ω B97X, ω B97XD (in Gaussian), B3LYP, B3PW91, B97-D3, B97M-rV, BLYP, M06-2X, M06-L, PBE, revPBE, revPBE0, TPSS, TPSSh, ω B97M-V, ω B97X, ω B97X-D, ω B97X-D3, ω B97X-V, wM05-D (in Q-Chem). These functionals were selected because they demonstrated high performance in various benchmark studies.^{6,8,14}

The list of screened basis sets included the following: Apr-cc-pV5Z, Apr-cc-pV6Z, Apr-cc-pVDZ, Apr-cc-pVQZ, Apr-cc-pVTZ, AUG-cc-pV5Z, AUG-cc-pV6Z, AUG-cc-pVDZ, AUG-cc-pVQZ, AUG-cc-pVTZ, aug-pc-3, aug-pc-4, aug-pcJ-3, aug-pcJ-4, aug-pcS-3, aug-pcS-4, aug-pcseg-3, aug-pcseg-4, CBSB7, cc-pV5Z, cc-pV6Z, cc-pVDZ, cc-pVQZ, cc-pVTZ, CEP-121G, CEP-31G, CEP-4G, D95, D95V, dAug-cc-pV5Z, dAug-cc-pV6Z, dAug-cc-pVDZ, dAug-cc-pVQZ, dAug-cc-pVTZ, Def2QZV, Def2QZVP, Def2QZVPP, Def2SV, Def2SVP, Def2SVPP, Def2TZV, Def2TZVP, Def2TZVPP, DGDZVP, DGDZVP2, DGTZVP, EPR-II, EPR-III, Jul-cc-pV5Z, Jul-cc-pV6Z, Jul-cc-pVDZ, Jul-cc-pVQZ, Jul-cc-pVTZ, Jun-cc-pV5Z, Jun-cc-pV6Z, Jun-cc-pVDZ, Jun-cc-pVQZ, Jun-cc-pVTZ, LanL2DZ, LanL2MB, May-cc-pV5Z, May-cc-pV6Z, May-cc-pVDZ, May-cc-pVQZ, May-cc-pVTZ, MidiX, MTSmall, pc-3, pc-4, pcJ-3, pcJ-4, pcS-3, pcS-4, pcseg-3, pcseg-4, QZVP, SDD, SDDAll, SHC, spAug-cc-pV5Z, spAug-cc-pV6Z, spAug-cc-pVDZ, spAug-cc-pVQZ, spAug-cc-pVTZ, STO-3G, SV, SVP, TApr-cc-pV5Z, TApr-cc-pV6Z, TApr-cc-pVDZ, TApr-cc-pVQZ, TApr-cc-pVTZ, TJul-cc-pV5Z, TJul-cc-pV6Z, TJul-cc-pVDZ, TJul-cc-pVQZ, TJul-cc-pVTZ, TJun-cc-pV5Z, TJun-cc-pV6Z, TJun-cc-pVDZ, TJun-cc-

pVQZ, TJun-cc-pVTZ, TMay-cc-pV5Z, TMay-cc-pV6Z, TMay-cc-pVDZ, TMay-cc-pVQZ, TMay-cc-pVTZ, TZV, TZVP, UGBS, UGBS1O, UGBS1P, UGBS1V, UGBS2O, UGBS2P, UGBS2V, UGBS3O, UGBS3P, UGBS3V, 3-21G, 4-31G, 6-21G, 6-311+G, 6-311G, 6-31G (in Gaussian), aug-cc-pCV5Z, aug-cc-pCVDZ, aug-cc-pCVQZ, aug-cc-pCVTZ, aug-cc-pV5Z, aug-cc-pVDZ, aug-cc-pVQZ, aug-cc-pVTZ, aug-pc-1, aug-pc-2, aug-pc-3, aug-pc-4, aug-pcS-0, aug-pcS-1, aug-pcS-2, aug-pcS-3, aug-pcS-4, aug-pcseg-0, aug-pcseg-1, aug-pcseg-2, aug-pcseg-3, aug-pcseg-4, cc-pCV5Z, cc-pCVDZ, cc-pCVQZ, cc-pCVTZ, cc-pV5Z, cc-pVDZ, cc-pVQZ, cc-pVTZ, crenbl, def2-QZVP, def2-QZVPD, def2-QZVPP, def2-QZVPPD, def2-SVP, def2-SVPD, def2-TZVP, def2-TZVPD, def2-TZVPP, def2-TZVPPD, DZ, DZ+, DZ++, G3LARGE, G3MP2LARGE, hwmb, lacvp, lanl2dz, lanl2dz-sv, pc-0, pc-1, pc-2, pc-3, pc-4, pcJ-0, pcJ-1, pcJ-2, pcJ-3, pcJ-4, pcS-0, pcS-1, pcS-2, pcS-3, pcS-4, pcseg-0, pcseg-1, pcseg-2, pcseg-3, pcseg-4, r64G, racc-pVDZ, racc-pVQZ, racc-pVTZ, rcc-pVQZ, rcc-pVTZ, sbkjc, srlc, srsc, STO-2G, STO-3G, STO-6G, SV, TZ, TZ+, TZ++, TZV, UGBS, VDZ, VTZ, 3-21+G, 3-21G, 4-31G, 6-31+G, 6-311+G, 6-311G, 6-31G (in Q-Chem).

In total, for DFT, we obtained nontrivial results for 1259 combinations of a functional and a basis set in Gaussian, and 1744 combinations in Q-Chem (two lists of combinations partially overlapped). For MP2, we successfully ran computations for at least one molecule out of six with 97 basis sets, and for CCSD, with 86 basis sets. These numbers exclude screened combinations of functionals and basis sets (for DFT) or basis sets (for MP2 and CCSD) for which quantum chemical computations have not converged for various reasons [e.g., insufficient wallclock time (up to 2 days allocated), insufficient memory, not diverged SCF iterations, etc.].

$L1$ measures reported in Tables S1 and S2 were computed as follows. Cube files for two compared combinations of method and basis set were calculated, either from fchk files (as described) or directly (CCSD and MP2 computations in Q-Chem), with the same size, position and orientation of the grids as for the reference electron densities. After that, differences of two cube files were computed with cubman utility from Gaussian, and sums of absolute values of all elements in each difference cube files were computed with a simple C++ code written by us. The values of the integral in $L1$ measure were computed as the products of sums of all values multiplied by the grid spacing cubed (essentially, with a 3D generalization of the rectangle rule). Simultaneously, an integral of each electron density over the whole cube was computed to check the accuracy of such integration and the sufficiency of the cube size. We tried different grid spacings and concluded that 0.1 bohr (but not 0.2 bohr) is sufficient to get at least two correct significant figures in the values of $L1$ measures (data not shown). With this grid spacing, it is sufficient to use a $161 \times 161 \times 161$ grid to fit any of six molecules shown in Table S1 and S2.

To compute the effective time shown in Fig. S2, we ran DFT computations for each combination of a functional and basis set for QM9 entries 8 000, 16 000 and 32 000, as described above, and recorded total wallclock time for each computation to complete. Whenever possible, ratios of total times for molecules 16 000 and 8 000 were computed, and a median value of these ratios across all combinations of a functional and basis set was found. Similarly, a median value of the ratio of wallclock times for molecules 32 000 and 8 000 was computed. Finally, for every functional/basis set combination, the wallclock time for molecule 8 000, the wallclock time for 16 000 divided by the median for the 16000/8000 ratio, and the wallclock time for 32 000 divided by the median for the 32000/8000 ratio were computed whenever possible. The effective time for every functional/basis set combination was computed as a geometric average of those of three variables that were available.

A3. Illustration of the idea with Taylor series expansion

This Section provides an illustration for the analysis presented in Section S3.1 for a much simpler example of a function of a single scalar variable. Consider an infinitely differentiable real-valued function $y(x)$ of a real-valued variable x . Suppose we know the values of all derivatives $y(x)$ of at a certain value x_0 . Then, the values of y at any x within the radius of convergence can be found from the Taylor series:

$$y(x) = y(x_0) + y'(x_0)\Delta x + \frac{y''(x_0)}{2!}\Delta x^2 + \frac{y'''(x_0)}{3!}\Delta x^3 + \dots, \quad (\text{S30})$$

where $\Delta x = x - x_0$. Further, Eq. (S30) can be used to find all minima of $y(x)$ within the radius of convergence with an arbitrary accuracy as a function of the values of derivatives of $y(x)$ at x_0 only.

Cutting this series at the second order terms, we arrive at

$$y(x) \simeq y(x_0) + y'(x_0)\Delta x + \frac{y''(x_0)}{2!}\Delta x^2. \quad (\text{S31})$$

This equation is analogous to Eq. (S5) in Section S3. The corresponding minimum [assuming $y''(x_0) > 0$] is achieved at

$$y'(x_0) + y''(x_0)\Delta x = 0, \quad (\text{S32})$$

$$\Delta x = -\frac{y'(x_0)}{y''(x_0)}. \quad (\text{S33})$$

This equation corresponds to Eq. (S7) in Section S3. Cutting Eq. (S30) at the third-order term, we get a more accurate approximation:

$$y(x) \simeq y(x_0) + y'(x_0)\Delta x + \frac{y''(x_0)}{2!}\Delta x^2 + \frac{y'''(x_0)}{3!}\Delta x^3. \quad (\text{S34})$$

At the local minimum, the following condition is satisfied:

$$y'(x_0) + y''(x_0)\Delta x + \frac{y'''(x_0)}{2}\Delta x^2 = 0. \quad (\text{S35})$$

This equation has two solutions:

$$\Delta x = -\frac{y''(x_0)}{y'''(x_0)} \left[1 \pm \sqrt{1 - \frac{2y'(x_0)y'''(x_0)}{(y''(x_0))^2}} \right]. \quad (\text{S36})$$

In the limit of $y'''(x_0) \rightarrow 0$, the solution with the plus sign diverges, while the solution with the minus sign approaches the right hand side of Eq. (S33), following the asymptotic expansion given below:

$$\Delta x = -\frac{y'(x_0)}{y''(x_0)} - \frac{(y'(x_0))^2}{2(y''(x_0))^3} y'''(x_0) + O\left((y'''(x_0))^2\right). \quad (\text{S37})$$

This result corresponds to Eq. (S9) in Section S3. Note that Eq. (S37) can also be obtained by rearranging Eq. (S35) in the following way:

$$y''(x_0)\Delta x = -y'(x_0) - \frac{y'''(x_0)}{2}\Delta x^2, \quad (\text{S38})$$

$$\Delta x = -\frac{y'(x_0)}{y''(x_0)} - \frac{y'''(x_0)}{2y''(x_0)}\Delta x^2, \quad (\text{S39})$$

rewriting it in an iterative form:

$$\Delta x_{n+1} = -\frac{y'(x_0)}{y''(x_0)} - \frac{y'''(x_0)}{2y''(x_0)}\Delta x_n^2, \quad (\text{S40})$$

using the approximate solution, Eq. (S33), as the initial value for iterations Δx_0 , and carrying out one iteration with Eq. (S40). This approach [unlike the asymptotic expansion of Eq. (S36) leading to Eq. (S37)] can be directly generalized from the analysis of a real-valued function $y(x)$ to the density functionals as given in Section S3.

To sum up, for an infinitely differentiable real-valued function of a real-valued variable, to find a minimum of the function, it is sufficient to know the values of the derivatives only at a certain point x_0 is close enough to the minimum (more strictly, such that the minimum is within the radius of convergence of the expansion about x_0). Our analysis in Section 3 generalizes this simple result to the density functional $E[\cdot]$ in Quantum Chemistry.

A4. Data availability

The fchk files for all QM9 molecules computed with PBE0/pcS-3 and HF/pcS-3, as well as a file with the corresponding energies, are available from Stanford Digital Repository by the following link: <https://purl.stanford.edu/kf921gd3855> The code for the DNN (in Tensorflow) and the cube files used for training will be made publically available after the paper is accepted.

References for the SI

- 1 Landau, L. D. & Lifshits, E. M. *Quantum mechanics, non-relativistic theory*. (Pergamon Press; Addison-Wesley Pub. Co., 1958).
- 2 Hohenberg, P. & Kohn, W. Inhomogeneous Electron Gas. *Phys. Rev.* **136**, B864 (1964).
- 3 Koch, W. & Holthausen, M. C. *A chemist's guide to density functional theory*. 2nd ed, (Wiley-VCH, 2001).
- 4 Becke, A. D. Perspective: Fifty years of density-functional theory in chemical physics. *J. Chem. Phys.* **140**, 18A301, doi:10.1063/1.4869598 (2014).
- 5 Jones, R. O. Density functional theory: Its origins, rise to prominence, and future. *Rev. Mod. Phys.* **87**, 897 (2015).
- 6 Mardirossian, N. & Head-Gordon, M. Thirty years of density functional theory in computational chemistry: an overview and extensive assessment of 200 density functionals. *Mol. Phys.* **115**, 2315-2372 (2017).
- 7 Parr, R. G. & Yang, W. *Density-functional theory of atoms and molecules*. (Oxford University Press; Clarendon Press, 1989).
- 8 Medvedev, M. G., Bushmarinov, I. S., Sun, J., Perdew, J. P. & Lyssenko, K. A. Density functional theory is straying from the path toward the exact functional. *Science* **355**, 49-52, doi:10.1126/science.aah5975 (2017).
- 9 Chai, J. D. & Head-Gordon, M. Long-range corrected hybrid density functionals with damped atom-atom dispersion corrections. *Phys. Chem. Chem. Phys.* **10**, 6615-6620, doi:10.1039/b810189b (2008).
- 10 Lin, Y. S., Li, G. D., Mao, S. P. & Chai, J. D. Long-Range Corrected Hybrid Density Functionals with Improved Dispersion Corrections. *J. Chem. Theory Comput.* **9**, 263-272, doi:10.1021/ct300715s (2013).
- 11 Perdew, J. P., Burke, K. & Ernzerhof, M. Generalized Gradient Approximation Made Simple. *Phys. Rev. Lett.* **77**, 3865-3868, doi:10.1103/PhysRevLett.77.3865 (1996).
- 12 Adamo, C. & Barone, V. Toward reliable density functional methods without adjustable parameters: The PBE0 model. *J. Chem. Phys.* **110**, 6158-6169, doi:10.1063/1.478522 (1999).
- 13 Jensen, F. Basis Set Convergence of Nuclear Magnetic Shielding Constants Calculated by Density Functional Methods. *J. Chem. Theory Comput.* **4**, 719-727, doi:10.1021/ct800013z (2008).
- 14 Bleiziffer, P., Schaller, K. & Riniker, S. Machine Learning of Partial Charges Derived from High-Quality Quantum-Mechanical Calculations. *J. Chem. Inf. Model.* **58**, 579-590, doi:10.1021/acs.jcim.7b00663 (2018).
- 15 Kupka, T. *et al.* From CCSD(T)/aug-cc-pVTZ-J to CCSD(T) complete basis set limit isotropic nuclear magnetic shieldings via affordable DFT/CBS calculations. *Magn. Reson. Chem.* **49**, 231-236, doi:10.1002/mrc.2738 (2011).
- 16 Hedegard, E. D., Jensen, F. & Kongsted, J. Basis Set Recommendations for DFT Calculations of Gas-Phase Optical Rotation at Different Wavelengths. *J. Chem. Theory Comput.* **8**, 4425-4433, doi:10.1021/ct300359s (2012).
- 17 Reid, D. M., Kobayashi, R. & Collins, M. A. Systematic Study of Locally Dense Basis Sets for NMR Shielding Constants. *J. Chem. Theory Comput.* **10**, 146-152, doi:10.1021/ct4007579 (2014).
- 18 Ji, H. & Jung, Y. A local environment descriptor for machine-learned density functional theory at the generalized gradient approximation level. *J Chem Phys* **148**, 241742, doi:10.1063/1.5022839 (2018).
- 19 Payne, P. W. Density functionals in unrestricted Hartree-Fock theory. *J. Chem. Phys.* **71**, 490, doi:10.1063/1.438124 (1979).
- 20 Ronneberger, O., Fischer, P. & Brox, T. in *Medical Image Computing and Computer-Assisted Intervention – MICCAI 2015. MICCAI 2015. Lecture Notes in Computer Science* Vol. 9351 (eds Navab N, Hornegger J, Wells W, & Frangi A) (Springer, Cham, 2015).
- 21 Farimani, A. B., Gomes, J. & Pande, V. S. Deep Learning the Physics of Transport Phenomena. *arxiv*, 1709.02432v02431 (2017).
- 22 Faber, F. A. *et al.* Prediction Errors of Molecular Machine Learning Models Lower than Hybrid DFT Error. *J. Chem. Theory Comput.* **13**, 5255-5264, doi:10.1021/acs.jctc.7b00577 (2017).
- 23 Schutt, K. T. *et al.* SchNet: A continuous-filter convolutional neural network for modeling quantum interactions. *Adv. Neural Inf. Process. Syst.* **30**, 1-11 (2017).
- 24 Schutt, K. T., Arbabzadah, F., Chmiela, S., Müller, K. R. & Tkatchenko, A. Quantum-chemical insights from deep tensor neural networks. *Nat. Commun.* **8**, 13890, doi:10.1038/ncomms13890 (2017).
- 25 Collins, C. R., Gordon, G. J., von Lilienfeld, O. A. & Yaron, D. J. Constant size descriptors for accurate machine learning models of molecular properties. *J. Chem. Phys.* **148**, 241718, doi:10.1063/1.5020441 (2018).
- 26 Faber, F. A., Christensen, A. S., Huang, B. & von Lilienfeld, O. A. Alchemical and structural distribution based representation for universal quantum machine learning. *J. Chem. Phys.* **148**, 241717, doi:10.1063/1.5020710 (2018).
- 27 Gastegger, M., Schwiedrzik, L., Bittermann, M., Berzsenyi, F. & Marquetand, P. wACSF-Weighted atom-centered symmetry functions as descriptors in machine learning potentials. *J. Chem. Phys.* **148**, 241709, doi:10.1063/1.5019667 (2018).
- 28 Gubaev, K., Podryabinkin, E. V. & Shapeev, A. V. Machine learning of molecular properties: Locality and active learning. *J Chem Phys* **148**, 241727, doi:10.1063/1.5005095 (2018).
- 29 Kranz, J. J., Kubillus, M., Ramakrishnan, R., von Lilienfeld, O. A. & Elstner, M. Generalized Density-Functional Tight-Binding Repulsive Potentials from Unsupervised Machine Learning. *J Chem Theory Comput* **14**, 2341-2352, doi:10.1021/acs.jctc.7b00933 (2018).
- 30 Lubbers, N., Smith, J. S. & Barros, K. Hierarchical modeling of molecular energies using a deep neural network. *J Chem Phys* **148**, 241715, doi:10.1063/1.5011181 (2018).
- 31 Pronobis, W., Tkatchenko, A. & Müller, K. R. Many-Body Descriptors for Predicting Molecular Properties with Machine Learning: Analysis of Pairwise and Three-Body Interactions in Molecules. *J Chem Theory Comput* **14**, 2991-3003, doi:10.1021/acs.jctc.8b00110 (2018).
- 32 Schutt, K. T., Sauceda, H. E., Kindermans, P. J., Tkatchenko, A. & Müller, K. R. SchNet - A deep learning architecture for molecules and materials. *J. Chem. Phys.* **148**, 241722, doi:10.1063/1.5019779 (2018).

- 33 Unke, O. T. & Meuwly, M. A reactive, scalable, and transferable model for molecular energies from a neural network approach based on local information. *J. Chem. Phys.* **148**, 241708, doi:10.1063/1.5017898 (2018).
- 34 Smith, J. S. *et al.* Approaching coupled cluster accuracy with a general-purpose neural network potential through transfer learning. *Nature Commun.* **10**, 2903, doi:10.1038/s41467-019-10827-4 (2019).
- 35 Goodfellow, I., Bengio, Y. & Courville, A. *Deep learning*. (2015).
- 36 Tran, D., Bourdev, L., Fergus, R., Torresani, L. & Paluri, M. in *The IEEE International Conference on Computer Vision (ICCV)*, 4489-4497 (2015).
- 37 Wu, Z. *et al.* in *The IEEE Conference on Computer Vision and Pattern Recognition (CVPR)*, 1912-1920 (2015).
- 38 Charles, R. Q., Su, H., Kaichun, M. & Guibas, L. J. in *2017 IEEE Conference on Computer Vision and Pattern Recognition (CVPR)* (IEEE, Honolulu, HI, USA, 21-26 July 2017, 2017).
- 39 Goh, G. B., Hodas, N. O. & Vishnu, A. Deep learning for computational chemistry. *J. Comput. Chem.* **38**, 1291-1307, doi:10.1002/jcc.24764 (2017).
- 40 Butler, K. T., Davies, D. W., Cartwright, H., Isayev, O. & Walsh, A. Machine learning for molecular and materials science. *Nature* **559**, 547-555, doi:10.1038/s41586-018-0337-2 (2018).
- 41 Huang, B., Symonds, N. O. & von Lilienfeld, O. A. The fundamentals of quantum machine learning. *arxiv*, 1807.04259v04252 (2018).
- 42 Rupp, M., von Lilienfeld, O. A. & Burke, K. Guest Editorial: Special Topic on Data-Enabled Theoretical Chemistry. *J Chem Phys* **148**, 241401, doi:10.1063/1.5043213 (2018).
- 43 von Lilienfeld, O. A. Quantum Machine Learning in Chemical Compound Space. *Angew. Chem. Int. Ed. Engl.* **57**, 4164-4169, doi:10.1002/anie.201709686 (2018).
- 44 Brockherde, F. *et al.* Bypassing the Kohn-Sham equations with machine learning. *Nat. Commun.* **8**, 872, doi:10.1038/s41467-017-00839-3 (2017).
- 45 Smith, J. S., Isayev, O. & Roitberg, A. E. ANI-1: an extensible neural network potential with DFT accuracy at force field computational cost. *Chem. Sci.* **8**, 3192-3203, doi:10.1039/c6sc05720a (2017).
- 46 Alred, J. M., Bets, K. V., Xie, Y. & Yakobson, B. I. Machine learning electron density in sulfur crosslinked carbon nanotubes. *Composites Science and Technology* **166**, 3-9, doi:10.1016/j.compscitech.2018.03.035 (2018).
- 47 Schmidt, E., Fowler, A. T., Elliott, J. A. & Bristowe, P. D. Learning models for electron densities with Bayesian regression. *Computational Materials Science* **149**, 250-258 (2018).
- 48 Bereau, T., DiStasio, R. A., Jr., Tkatchenko, A. & von Lilienfeld, O. A. Non-covalent interactions across organic and biological subsets of chemical space: Physics-based potentials parametrized from machine learning. *J. Chem. Phys.* **148**, 241706, doi:10.1063/1.5009502 (2018).
- 49 Nguyen, T. T. *et al.* Comparison of permutationally invariant polynomials, neural networks, and Gaussian approximation potentials in representing water interactions through many-body expansions. *J Chem Phys* **148**, 241725, doi:10.1063/1.5024577 (2018).
- 50 Imbalzano, G. *et al.* Automatic selection of atomic fingerprints and reference configurations for machine-learning potentials. *J. Chem. Phys.* **148**, 241730, doi:10.1063/1.5024611 (2018).
- 51 Wu, Z. *et al.* MoleculeNet: a benchmark for molecular machine learning. *Chem. Sci.* **9**, 513-530, doi:10.1039/c7sc02664a (2018).
- 52 Yao, K., Herr, J. E., Toth, D. W., McKintyre, R. & Parkhill, J. The TensorMol-0.1 model chemistry: a neural network augmented with long-range physics. *Chem. Sci.* **9**, 2261-2269, doi:10.1039/c7sc04934j (2018).
- 53 Smith, J. S., Nebgen, B., Lubbers, N., Isayev, O. & Roitberg, A. E. Less is more: Sampling chemical space with active learning. *J. Chem. Phys.* **148**, 241733, doi:10.1063/1.5023802 (2018).
- 54 Zaspel, P., Huang, B., Harbrecht, H. & von Lilienfeld, O. A. Boosting quantum machine learning models with multi-level combination technique: Pople diagrams revisited. *arxiv*, 1808.02799v02792 (2018).
- 55 Yao, K. & Parkhill, J. Kinetic Energy of Hydrocarbons as a Function of Electron Density and Convolutional Neural Networks. *J. Chem. Theory Comput.* **12**, 1139-1147, doi:10.1021/acs.jctc.5b01011 (2016).
- 56 Seino, J., Kageyama, R., Fujinami, M., Ikabata, Y. & Nakai, H. Semi-local machine-learned kinetic energy density functional with third-order gradients of electron density. *J. Chem. Phys.* **148**, 241705, doi:10.1063/1.5007230 (2018).
- 57 Hollingsworth, J., Li, L., Baker, T. E. & Burke, K. Can exact conditions improve machine-learned density functionals? *J Chem Phys* **148**, 241743, doi:10.1063/1.5025668 (2018).
- 58 Golub, P. & Manzhos, S. Kinetic energy densities based on the fourth order gradient expansion: performance in different classes of materials and improvement via machine learning. *arxiv*, 1805.10855v10852 (2018).
- 59 Nagai, R., Akashi, R., Sasaki, S. & Tsuneyuki, S. Neural-network Kohn-Sham exchange-correlation potential and its out-of-training transferability. *J Chem Phys* **148**, 241737, doi:10.1063/1.5029279 (2018).
- 60 Szegedy, C. *et al.* Intriguing properties of neural networks. *arxiv*, 1312.6199v1314 (2013).
- 61 Kurakin, A., Goodfellow, I. & Bengio, S. Adversarial examples in the physical world. *arxiv*, 1607.02533v02534 (2016).
- 62 Nebgen, B. *et al.* Transferable Dynamic Molecular Charge Assignment Using Deep Neural Networks. *J. Chem. Theory Comput.* **14**, 4687-4698, doi:10.1021/acs.jctc.8b00524 (2018).
- 63 Sifain, A. E. *et al.* Discovering a Transferable Charge Assignment Model Using Machine Learning. *J. Phys. Chem. Lett.* **9**, 4495-4501, doi:10.1021/acs.jpcllett.8b01939 (2018).
- 64 Welborn, M., Cheng, L. & Miller III, T. F. Transferability in Machine Learning for Electronic Structure via the Molecular Orbital Basis. *arxiv*, 1806.00133v00132 (2018).

- 65 Margraf, J. T. & Reuter, K. Making the Coupled Cluster Correlation Energy Machine-Learnable. *J Phys Chem A* **122**, 6343-6348, doi:10.1021/acs.jpca.8b04455 (2018).
- 66 Ramakrishnan, R., Dral, P. O., Rupp, M. & von Lilienfeld, O. A. Quantum chemistry structures and properties of 134 kilo molecules. *Sci. Data* **1**, 140022, doi:10.1038/sdata.2014.22 (2014).
- 67 Nakata, M. & Shimazaki, T. PubChemQC Project: A Large-Scale First-Principles Electronic Structure Database for Data-Driven Chemistry. *J Chem Inf Model* **57**, 1300-1308, doi:10.1021/acs.jcim.7b00083 (2017).
- 68 Smith, J. S., Isayev, O. & Roitberg, A. E. ANI-1, A data set of 20 million calculated off-equilibrium conformations for organic molecules. *Sci. Data* **4**, 170193, doi:10.1038/sdata.2017.193 (2017).
- 69 Ghahremanpour, M. M., van Maaren, P. J. & van der Spoel, D. The Alexandria library, a quantum-chemical database of molecular properties for force field development. *Sci. Data* **5**, 180062, doi:10.1038/sdata.2018.62 (2018).
- 70 Feller, D. The Role of Databases in Support of Computational Chemistry Calculations. *J. Comp. Chem.* **17**, 1571-1586 (1996).
- 71 Schuchardt, K. L. *et al.* Basis set exchange: a community database for computational sciences. *J. Chem. Inf. Model.* **47**, 1045-1052, doi:10.1021/ci600510j (2007).